Impact of box-type floating breakwater on motion response of hydrodynamically coupled floating platforms downstream.

Arnav Doss

Master of Science Thesis

TU Delft

blue21

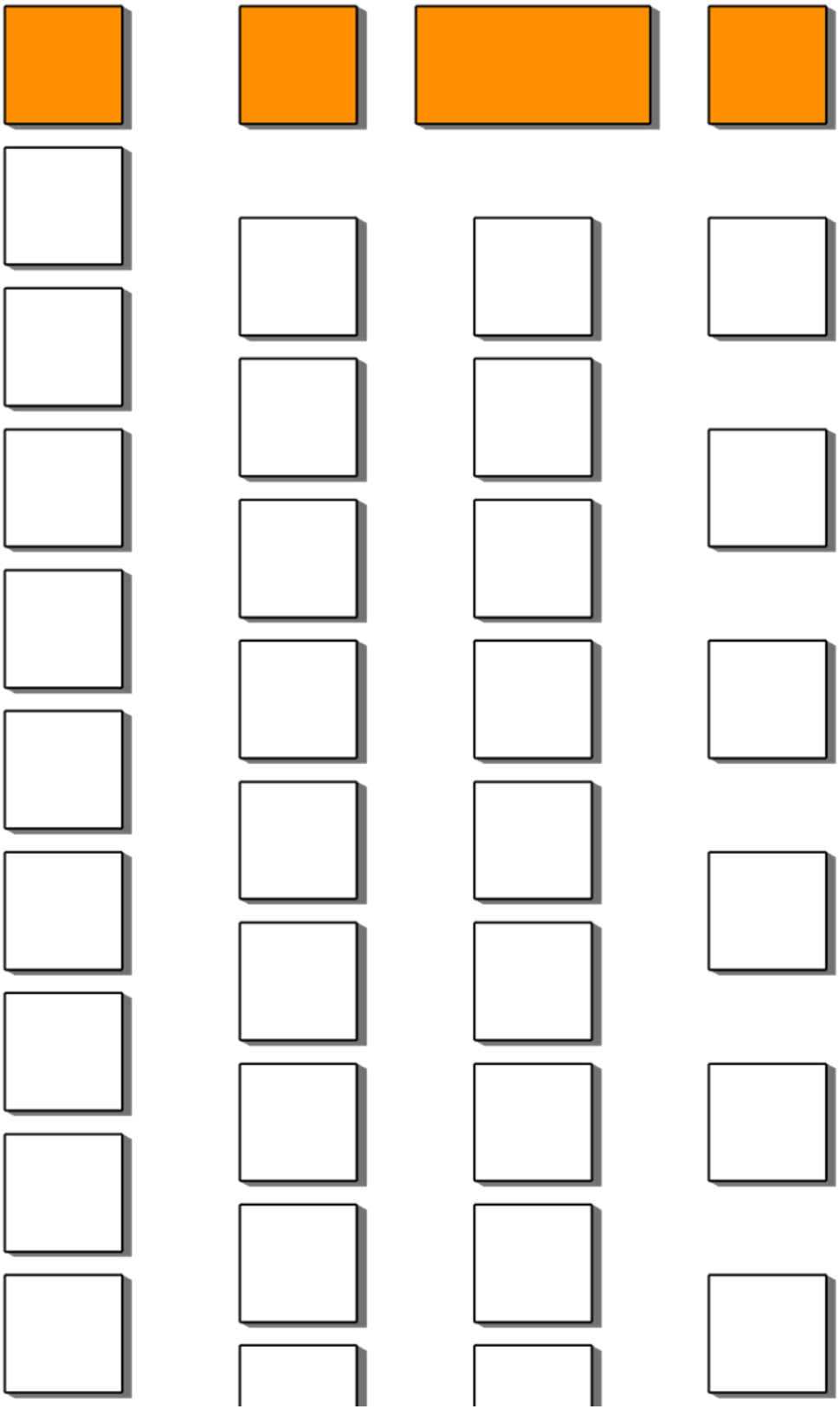

Impact of box-type floating breakwater on motion response of hydrodynamically coupled floating platforms downstream.

MASTER OF SCIENCE THESIS

Thesis for the degree of Master of Science in Offshore and Dredging Engineering

Faculty of Mechanical, Maritime and Materials Engineering

Delft University of Technology

Chairman of Graduation Committee: _____

Prof.dr.ir. J. Westerweel

Company Supervisor (Blue21): _____

Dr. Ir. Jan van Kessel

University Daily Supervisor: _____

Dr. -Ing. S. Schreier

Graduation Committee Member: _____

Dr. ir. A. Antonini

Arnav Doss

4723678

Delft, November 2020

The work elaborated on in this thesis was sponsored by Blue21

Abstract

Floating breakwaters are applicable in several offshore applications to protect downstream structures from excessive wave loads and to reduce their motion response. This thesis investigates the impact of the leading platform, functionally a breakwater, on the RAOs and response of the platforms behind it in frequency domain. The structures are only hydrodynamically coupled. All models were analysed for head waves only. Variables in model design are investigated using a combination of diffraction software and solving equations of motion in six degrees of freedom for each body. The variables are the gap between the breakwater and the first platform, the width, i.e. side perpendicular to wave direction, of the breakwater and the gap between platforms.

Base case dimensions for the platforms and breakwater are chosen based on the natural frequencies and wave transmission coefficients respectively. These choices are made to function well for the wave spectrum at the chosen site. Each case analysed included a breakwater and 10 platforms downstream of it.

It was found that he imperfect efficiency of a breakwater means that the first few platforms behind it act as breakwaters too; albeit for much lower wave energies. Increasing the gap between the breakwater and the first platform behind it results in a decrease in RAO of the platforms due to increasing hydrodynamic coupling. The impact on pitch RAOs is greater than the impact on the heave RAOs. Increasing the width of the breakwater results in minimal reduction in RAOs of the platforms behind it at large gap sizes. At small gap sizes, there is an adverse relationship. Hydrodynamic coupling between the platforms can lead to shared natural frequencies within the design frequency range, leading to a large motion response. This can be prevented by changing the gap size and thereby the hydrodynamic coupling and moving the natural frequency outside of the design range.

A breakwater and multiple platforms downstream of dimension $L = 100\ \mathrm{m}$, $B = 100\ \mathrm{m}$, $T = 5\ \mathrm{m}$, with a gap of $80\ \mathrm{m}$ between the breakwater and platforms and $100\ \mathrm{m}$ between the platforms themselves was shown to effectively reduce the motions of the downstream platforms.

The first few platforms exhibit higher heave than the other platforms, but similar pitch to the other platforms. Therefore, their use cases in a floating city must be chosen accordingly. The potential negative impacts of hydrodynamic coupling between the platforms means that the platforms must be further apart from each other, resulting in floating cities with a much larger footprint than previously expected. Further research into the motion response for 2D structure layout and different wave directions would be interesting follow-ups to this thesis.

Acknowledgements

This thesis took a lot longer than I had expected, but through the setbacks and changes in direction I have learned a lot. I hope you will enjoy reading this report.

I would like to thank my supervisor Dr. -Ing. S. Schreier for his guidance, support, and immense patience as I struggled through numerous setbacks. His commitment towards helping me has gotten me to the finish line.

I would also like to thank my company supervisor Dr. Ir. Jan van Kessel for inspiring me and helping me find joy in my work. His guidance and support during my internship and thesis have been invaluable.

I would also like to thank Drs. Evert Vixseboxse for his kindness and help. I have reached the end of my masters thanks to his support and sage advice.

Throughout my life, I have received unwavering love and support from my family. Their encouragement and trust in my abilities have helped me recognise and develop my own strengths. I would like to thank them for always being there for me. Finally, I would like to thank my friends for being supportive throughout my time at TUDelft.

Arnav Doss,

Delft, November 2020

Index of Contents

1. Introduction

The world is increasingly urban. Globally, an estimated three million people move to live in cities every week, with 68% of the world population expected to be urban by 2050 (United Nations, 2018). Almost all future increase in population is also expected to be in urban locations (Bravo, 2018). The challenge of meeting the needs of these new arrivals in a sustainable and ethical manner is immense.

The natural process of unplanned urban sprawl spreading out into the city outskirts have shown some benefits in the short term such as improved standards of living for the existing residents, but in the long term, the future costs will significantly outweigh the benefits (Gold, 2018).These unmanaged, unstructured urban expansions have been found to demand greatly increased funding requirements to meet basic urban infrastructure and services. The funding gap leads to many such cities failing to provide these to their citizens, greatly reducing any benefits of urban migration that might have been felt by the residents of the sprawl. Furthermore, these urban sprawls seem to lock-in inefficiencies with high levels of energy consumption, increased traffic congestion leading to escalating economic and social costs due to air pollution, increase social exclusion and a wide range of other economic and social costs (The New Climate Economy, 2014).

Providing basic infrastructure and services to its residents and reducing the climate impact of their cities are an ethical imperative for the governments. Urban sprawl makes that increasingly difficult for governments to achieve even if they have the political willpower to do so. The solution to providing better lives, not just for the urban migrants but all residents of the city is highly dense cities. Studies show that highly dense cities are able to provide to the needed infrastructure and services at much lower costs while being more environmentally friendly with greatly reduced climate impact in the long run (The New Climate Economy, 2014). However, empty land that can be designed from the ground up is hard to find in the cities already bursting to their limits.

As authorities around the world grapple with the challenge, one solution has increasingly received more interest. With 90% of the world's largest cities being situated on waterfronts, facing increasing risk from rising sea levels and flooding, a High-Level Round Table on Sustainable Floating Cities was held on April 2019 in New York by the United Nations Human Settlements Program. The discussion revolved around the use of floating cities to create sustainable, carbon-neutral cities that could tackle the issues of climate change, food & water scarcity and renewable energy head on using the latest technologies and a blank slate to design the most optimal cities (United Nations, 2019). The negative impacts of expanding into the city outskirts can be eliminated while allowing governments to meet their ethical imperatives to provide for their residents.

Blue21, a maritime urban project company that designs, researches and realises projects in cities world-wide. Blue21 is currently working on floating city solutions to meet these goals. One of the concepts proposed by Blue21 for The Netherlands is shown in Figure 1.1.

Figure 1.1 North Sea Topicon design concept [Source: Blue21]

Expanding cities into the sea is not a novel idea. Many of the largest cities on the planet have already been encroaching on the sea using reclaimed land. Approximately 20% of Singapore and 25% of Tokyo is built on reclaimed land. The Netherlands have famously more than doubled their available land area through land reclamation (Cosgrave, 2017). The ability to start fresh on a blank slate allows cities to effectively design sustainable extensions using the latest technologies and knowledge without having to compromise due to existing infrastructure, communities or features.

With a drastically reduced environmental impact and cost, floating cities provide a great alternative to reclaimed land (Wang & Tay, 2011). Floating platforms are considered more environmentally friendly as they float over the marine ecosystem. This means that the platforms do not contribute to the silting up of deep harbours, are impervious to seismic shocks and quick & easy to construct, install, remove or expand (Wang, et al., 2006). Furthermore, floating cities can be modular, adapting to changes in needs and populations over time while being able to weather rising sea levels. The concept of floating cities envisions not just habitation, but industry and agriculture offshore as well. Floating farms, factories, commercial spaces and offices are integral to creating a sustainable city that can meet the growing demands without overburdening the existing infrastructure and keeping its carbon footprint in check. Some examples of such uses are floating greenhouses, solar farms, container ports and airports. The purely economic need to create infrastructure resilient to sea level rise also increases interest in floating cities. Many potential uses are already in their pilot stages.

The crux for all these ideas is the floating platform upon which they will be built. Over the last few decades, work on developing such platforms has slowly progressed. From military research into Mobile Offshore Bases (ABS, 1999) to commercial ventures such as floating hotels and airports. The immense technical challenges have been resolved one by one, but there is still a lot of work to be done.

One recent project is the SPACE@SEA project funded under the European Union's Horizon 2020 programme to develop a standardised and cost-efficient modular island for work and living with low ecological impact. A consortium of 17 European partners including Blue21 endeavoured to deliver on this vision. Figure 1.2 shows one of the platform designs being tested at the Maritime Research Institute Netherlands (MARIN).

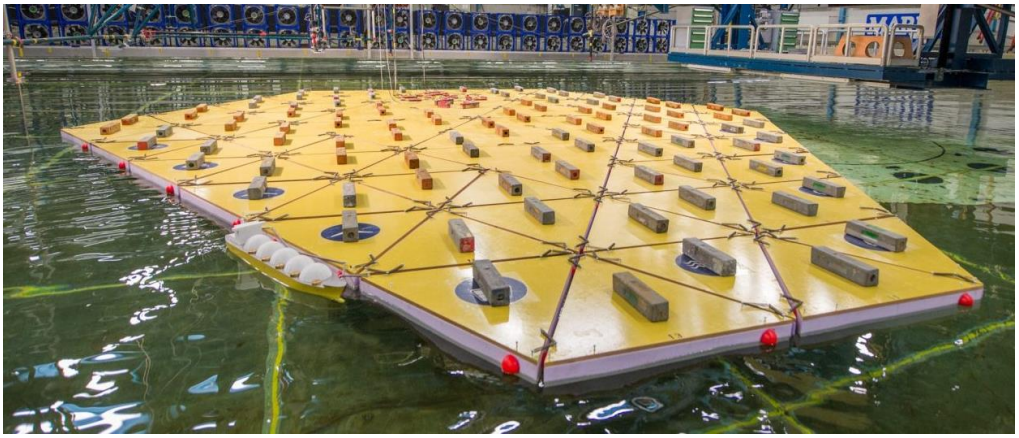

Figure 1.2 SPACE@SEA Project [Source: MARIN]

In order to meet the design challenges of this revolutionary idea, Blue21 looks at design, sustainability and technology together. Blue21 hopes to kick-start the Blue Revolution by working with other leading experts in the field of maritime and offshore engineering. Figure 1.3 shows a pilot project planned by Blue21 in this field. While the architects, designers and sustainability experts work on designing cities to match the criteria, offshore engineers are needed to study the technical feasibility of such projects.

In brief, as urban migration rises and the necessity to act against climate change becomes more pressing, governments must provide infrastructure and services to their residents in an ethical, equitable and ecologically sound manner. Expanding cities onto thoroughly planned, highly dense floating platforms provides a promising solution to achieve all these goals.

Figure 1.3 Floating Island in French Polynesia [Source: Blue21]

1.1. Brief Analysis of Problem

Ideally, to function as a city, there is a need for large platforms on the order of 200-300m that might act as city blocks that are then placed next to each other like in a terrestrial city. Since, these structures are designed to stay in one place, they need not be hydrodynamically streamlined like ships. Therefore, they can have large, flat bottoms. Since the submerged volume can be spread out over a large bottom surface area, such structures generally have relatively small drafts. Structures of large dimensions with flat bottoms and shallow drafts are classified as Very Large Floating Structures (VLFS). VLFS and their unique characteristics are an established field of research, the learnings of which can be applied to the subjects of this thesis.

However, given the nascent state of such concepts, industry players must begin with relatively smaller platforms of around 100m, the number of which in a location/project may be increased as interest and investments rise. Logistical, manufacturing, and technical considerations put further downward pressure on the sizes of individual platforms. Learnings from research into VLFS can still be applied to the smaller platforms because they share the primary characteristic of a relatively shallow draft and flat bottoms (Wang, et al., 2006).

The primary design goals for such structures are survival and minimal motions in design sea states. Motion sickness on vessels is closely related to the heave of the vessel, with roll and sway showing no such correlation (Lawther & Griffin, 1988). Reducing the magnitude of heave oscillations at frequencies of $0.125 - 0.25$ Hz ($0.76 - 1.57$ rad/s), or reducing the time of exposure to such oscillations would be expected to reduce the incidence of seasickness. Furthermore, the root mean square heave accelerations should be limited to $0.02\ g$ where g is the gravitational acceleration (Riola & Garcia de Arboleya, 2006). However, a large surface area and small draft results in large motions and hydroelastic behaviour requiring the need for adjacent breakwaters if one wants to keep motions and deflections to a minimum (Wang, et al., 2010). Therefore, the concept of having multiple smaller platforms protected by a breakwater is a more realistic vision, at least in the near future.

One of the most effective methods of reducing the hydroelastic response of the VLFS is by reducing the wave energy hitting it. Thereby, one of the earliest methods was using a bottom-founded breakwater which is effecting in reducing hydroelastic response and drift forces as shown by (Utsunomiya, et al., 2001; Ohmatsu, 1999). The drawbacks with bottom-founded breakwaters are large capital expenditure, environmental impact and material requirements, difficult construction and wave reflection that could erode coastlines (Wang & Tay, 2011). Floating breakwaters have therefore been the area of research over the last few decades since they do not damage the seabed, do not disrupt ocean current flow, and have potential uses as collision protection or oil spill barriers.

The impact of these floating breakwaters on platforms downstream of them needs to be studied to determine the viability of a design. Although a lot of work has been done on individual floating breakwaters and their effectiveness is reducing transference of wave energy, few studies have been done on their impact beyond the bodies just behind it. The little work

done on this topic is restricted to one or two connected platforms using model tests, thereby providing no numerical method to simulate such systems. It is only in the last few years that interest in looking at such coupled systems and their dynamics using numerical methods has increased. Therefore, there is a gap in research that needs to be fulfilled before the concept of floating cities can be realised. This thesis aims to begin filling this gap by starting with the hydrodynamic coupling between the floating breakwater and multiple platforms downstream.

1.2. Final objective

The final objective of this thesis is to find an effective breakwater configuration. To achieve this objective, the impact of a floating breakwater (the leading module) on the RAOs and response of the series of platforms downstream of the breakwater must be analysed. Figure 1.4 shows an idealized module configuration where the floating breakwater is shown in orange. The dotted lines show some of the variable position and dimensions of the breakwater and platforms that will be studied. They are increasing the width of the breakwater, changing its distance to the other platforms, and changing the distance (gap) between the platforms themselves. There is a need to develop a tool first that can execute the desired case studies and provide the desired outputs.

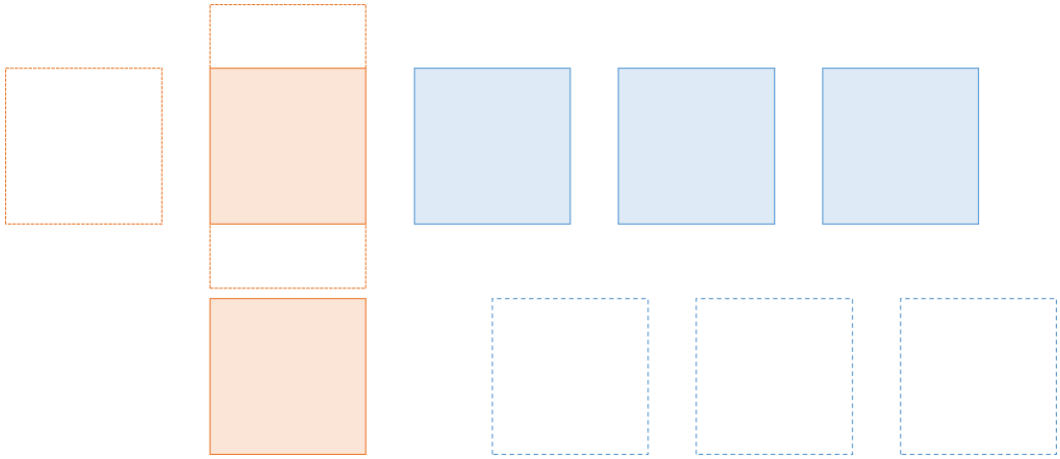

Figure 1.4: Idealized Module Configuration with floating breakwater (orange) and floating platforms (blue)

1.3. Research question

The problem being studied can be condensed into a single research question.

"What is the impact of the gap between platforms and the leading modules' width & gap distance on the motion response of the floating platforms downstream to it?"

2. Very Large Floating Structures (VLFS)

As stated in the brief analysis of the problem, the structures being studied in this thesis can be classified as Very Large Floating Structures (VLFS) owing to their defining characteristic of relatively shallow drafts. Although, smaller than the structures of 1000m length theorized by the coiner of the term VLFS (Suzuki, et al., 2006), many of the problems facing 1000m platforms are shared by the 100m platforms being studied in this thesis due to their shared characteristic of relatively shallow drafts (Wang, et al., 2006).

VLFS type structures were first introduced by Edward Armstrong around the 1920's as stepping-stones for aircraft flying across the oceans. However, the first non-stop transatlantic flight in 1927 by Charles Lindbergh dampened the interest in the concept. The concept saw no use outside of a few military experiments until the 1970's when the Japanese developed the concept for an extension for the Kansai International Airport and floating cities. A test runway, called the Mega Float, was constructed and placed in the Tokyo Bay in 1995 (Department in Shipbuilding Research Centre of Japan (SRC), 2003). These and other projects have provided important data for continued research into VLFS.

2.1. Short summary of relevant research into Hydroelastic Response of VLFS

VLFS in their simplest forms are large pontoons floating on the sea surface. Due to their large surface areas and relatively small depth, they behave elastically under wave action. There are two approaches to performing a hydroelastic response analysis, time-domain and frequency domain.

Frequency domain gives a hydroelastic response amplitude operator that captures the pertinent response parameters in a steady state condition. In this approach, a boundary value for solving the motion of the floating body is derived from the Laplace equation for the velocity potential. The boundary conditions correspond to the wetted surfaces, the Neumann condition at the seabed, the linearized free surface condition and the radiation conditions at infinity. The earliest such solution was proposed in (John, 1949; John, 1950) where Green's function was used to solve for the wave scattering. Linear wave theory was fully described by (Wehausen & Laitone, 1960). These early works looked at the floating body as a rigid structure. As interest in VLFS has grown, hydroelastic analysis has also gained attention; the pioneers of which include (Mamidipudi & Webster, 1994; Yago & Endo, 1996; Utsunomiya, et al., 1998; Kashiwagi, 1998; Ohmatsu, 1999).

Modelling VLFS as plates (Utsunomiya, et al., 1998; Kashiwagi, 1998; Watanabe, et al., 2000), time domain approaches (Watanabe, et al., 1998; Ohmatsu, 1998; Kashiwagi, 2004) and computational fluid dynamic (CFD) methods have also been focus areas for research into the hydroelastic response of VLFS.

Clearly, a lot of research has gone into understanding and modelling the hydroelastic response of the VLFS. However, it must be noted that multi-body systems have not had a lot of focus. This thesis begins with hydrodynamic response of multi-body systems as its focus and will

begin with rigid bodies. The designed method may act as a foundation on which further work on hydroelastic response of each body within the system can be added.

2.2. Mitigation of Hydroelastic Response using Breakwaters

There are many types of wave mitigating devices that can be attached to the VLFS structure. Some examples are submerged horizontal plates (Ohta, 1999; Watanabe, et al., 2003), vertical plates (Ohta, 1999), submerged boxes (Takagi, et al., 2000), oscillating water columns (Maeda, et al., 2000; Ikoma, et al., 2002; Hong, et al., 2006), air-cushion modules (van Kessel & Pinkster, 2007; Ikoma, et al., 2009) and hybrid systems (Shigemitsu, et al., 2001). A thorough literature review on the methods of mitigating hydroelastic response of VLFS under wave action can be found in (Wang, et al., 2010).

Floating Breakwaters

Box-type floating breakwaters are the simplest type of floating breakwaters. They are named as such owing to their simple shape. This type of breakwater has been well researched and investigated. A lot is known about their construction and response characteristics. Furthermore, important to floating cities is the ability to use these breakwaters as multi-use platforms. For example, they may be used for storage while still functioning as a breakwater. Therefore, the box-type floating breakwater has been chosen for this thesis.

These are floating boxes that attenuate incoming waves primarily through reflecting. They can be held in place by mooring lines, piles or dolphins. Figure 2.1 shows a sketched example of a box-type floating breakwater.

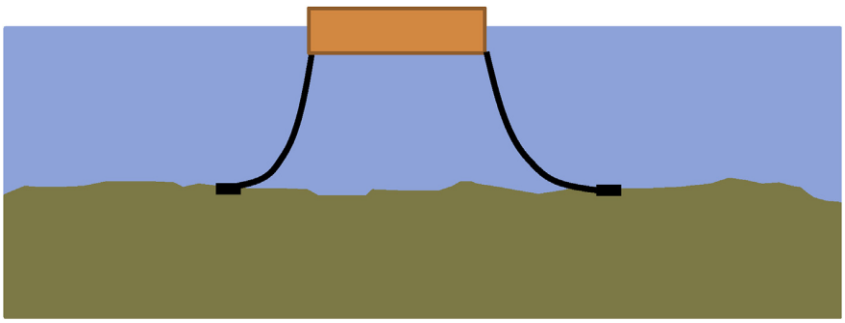

Figure 2.1 Sketch of box-type floating breakwater [Source: (Dai, et al., 2018)]

The simple geometry has led to theoretical formulae being derived for its wave transmission coefficient [k_t] since the 1950's (Dai, et al., 2018). A review of various studies on such breakwaters has shown that the effectiveness of such breakwaters are highly dependant on their length to wavelength [L/λ] ratio, where the length refers to the side length that is parallel to the wave direction. In order to achieve $k_t < 0.5$, L/ λ usually needs to exceed 0.35. Therefore, narrow breakwaters are almost transparent to long waves (Wang, et al., 2010). Studies by (Hong, et al., 2002; Tay, et al., 2009) have shown that the hydroelastic response of VLFS protected by box-type breakwaters are reduced by upto 70%.

In order to determine if hydroelasticity will have a large influence on the motions of the platforms and breakwater, the characteristic length of the structure can be calculated using the

equations below where λ_c is the characteristic length, EI is the bending stiffness and k_c is the spring constant of the hydrostatic restoring force (Suzuki, et al., 2006). If the characteristic length of the structure is greater than the wavelength, then the structure behaves like a rigid body and hydroelasticity can be safely neglected.

$$\lambda_c = 2\pi \left(\frac{EI}{k_c}\right)^{1/4} \tag{2.1}$$

The hydrostatic restoring force can be calculated for a structure, assuming longitudinal bending, using the equation below where B is the width of the structure.

$$k_c = \rho g B \tag{2.2}$$

For a box type structure of height H, top and bottom plates of thickness t and ignoring any side plating or internal plating, the bending stiffness EI can be estimated using the equation below where E refers to the Young's modulus.

$$EI = \left(\frac{1}{12} E(H^3 - (H - 2t)^3)\right) B \tag{2.3}$$

Assuming a steel structure of $B = 100\,\text{m}$, $t = 10\,\text{mm}$ and $H = 10\,\text{m}$, the characteristic length is $627\,\text{m}$. Therefore, as long as such a structure is floating in sea conditions with wavelengths less than $627\,\text{m}$, the structure can be assumed to be rigid. Since this thesis will focus on platforms that are around $100\,\text{m}$, and potential sites are unlikely to have wavelengths on the order of $600\,\text{m}$, the choice to neglect hydroelasticity has been taken.

Two floating long boxes arranged side-by-side were also studied based on the 2-D potential theory by (Williams, et al., 2000). Numerical parametric studies revealed that the geometry of and the spacing between the two floating boxes as well as the mooring line stiffness are the key factors that affect the performance of the floating breakwater. Figure 2.2 shows the studied setup.

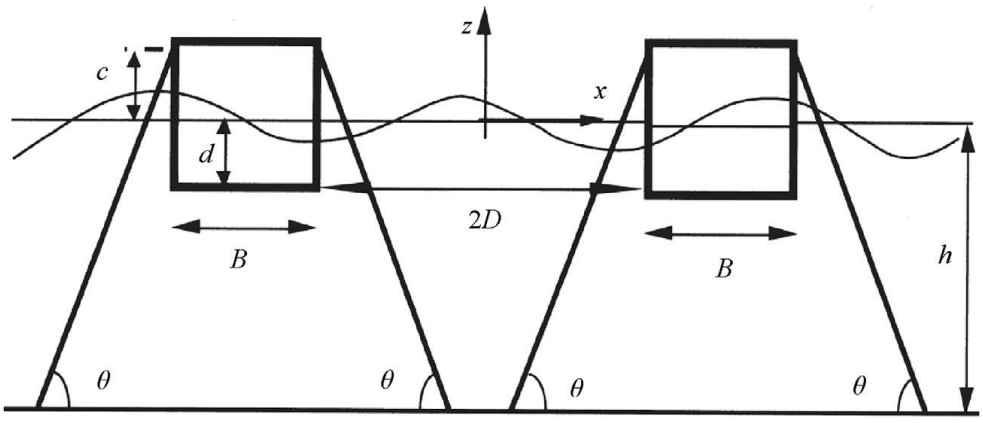

Figure 2.2 Floating double-box breakwater [Source: (Williams, et al., 2000)]

It was found that narrow spacing is effective in reflecting long waves as it acts like a single larger box and larger spacing is effective in reflecting short waves as it acts like two individual boxes in sequence. Furthermore, reducing mooring line stiffness resulted in more effective

reflection of long waves, but in a narrow frequency band of acceptable performance. Mooring line stiffness is only consequential in short waves if the mooring lines are too soft to restrain the motion of the breakwater. Therefore, dual-box breakwater may outperform a single box-type breakwater given the same overall dimensions (Williams, et al., 2000).

Gap resonance could be important when looking at oblique or beam waves. (Elchahal, et al., 2009) showed that resonance is expected if the length of the gap is around $(n \times \lambda)/2$, where n is an integer and λ is the wavelength.

Drift forces & mooring system design

Apart from the forces in the wave frequency, waves also have second-order effects called wave drift forces which are the design basis for mooring system. Two common methods are the near-field method (Pinkster, 1979) and the far-field method based on momentum-conservation (Maruo, 1960; Kagemoto & Yue, 1986; Utsunomiya, et al., 2001). Although both methods are reasonably accurate for single bodies, the far-field method has limitations when considering multiple adjacent floating modules due to it outputting only the total forces acting on all modules together rather than the individual forces on each module as outputted by the near-field method. However, the near field method requires quite complex computations in such a case. (Kashiwagi, et al., 2005) adopted the near-field method to compute the interaction of two adjacent ships in waves. The results of the study showed good agreement with experimental results.

There is a lot of research done into mooring systems. It is worth noting that for barge type structures, the main contributor to system stability is the large waterplane area which produces a large restoring moment in response to the platform rotations (Al-Solihat & Nahon, 2015). Furthermore, VLFS structures with shallow drafts feel little to no effects of currents and their environmental loading is dominated by the waves.

It should be noted that the second order drift forces and mooring are not important in this thesis as it focuses on the reduction in Response Amplitude Operator (RAO) rather than values like maximum excursion or mooring loads. The RAO relates to the wave frequency response, and therefore the long-term drift of the platforms does not impact the values being studied. Mooring systems, especially slack mooring like those used for VLFS, are designed to counteract drift only. They do not substantially impact the first order responses that are being studied in this thesis. These reasons lead to the choice of neglecting drift forces and mooring in this thesis.

3. Method

This thesis aims to study the influence of the floating breakwater on the motions of several floating structures downstream of the breakwater. All the floating structures are treated as free-floating rigid bodies, which are neither moored nor mechanically coupled to each other. They are only hydrodynamically coupled through radiated waves and diffraction. The influence of the breakwater on the motion of the downstream structures is assessed by computing the motion RAOs of the downstream structures for the different breakwater configurations. RAOs can be calculated by solving the equation of motion (EOM) for these bodies in frequency domain as shown in Figure 3.1. The variable descriptions and dimensions are shown in Table 3.1.

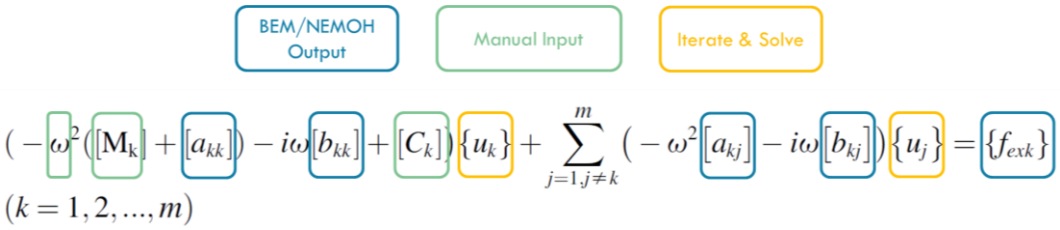

Figure 3.1: Equation of Motion of hydrodynamically coupled bodies and the source of its inputs.

The RAO's are the magnitude of u_k and u_j scaled by the wave amplitude. Therefore, by solving for those values in the EOM, one can achieve the aim of this thesis. As shown in Figure 3.1, some of the terms in the EOM come from BEM/NEMOH output. This refers to the outputs that an external software solves. This external software is used to reduce the complexity of this thesis and save time. Since the bodies being studied have large volumes relative to the waves, the impact of the fluid field can be determined by solving diffraction problems. Diffraction problems can be approached by using analytical methods for simple geometries. However, for more complex geometries, a numerical solver is better. The most common numerical approach to diffraction problems is the Boundary Element Method (BEM), the mathematical basis of which has been introduced in Appendix A. The BEM software used in this thesis is called NEMOH.

BEM / NEMOH

Considering the focus on hydrodynamic coupling, diffraction software packages comes to mind. There are many commercial diffraction packages, such as DELFRAC, ANSYS AQWA®, HydroStar® and WAMIT®, that are commonly used in academic research and commercial applications. However, due to the budgetary constraints of a start-up such as Blue21, only software that is free to use for commercial applications are viable options, hence the need for open-source software. Fortunately, there is one open-source diffraction software available that can handle multi-body analysis called NEMOH. This software coupled with a MATLAB® based post-processing script written for the task complete the tool. To maintain the open-source nature of the project, a MATALB® clone called OCTAVE has been used.

Table 3.1: EOM variable descriptions and dimensions

Variable	Dimension	Description
m	*Scalar*	Total number of floating bodies being analysed
$\boldsymbol{\omega}$	*Scalar*	Wave frequency
$\boldsymbol{M_k}$	6×6	Mass (or inertia moment) matrix of the kth submodule
$\boldsymbol{a_{kk}}$	6×6	Added mass matrix of the kth submodule caused by the motion of the submodule itself
$\boldsymbol{b_{kk}}$	6×6	Radiation damping matrix of the kth submodule caused by the motion of the submodule itself
$\boldsymbol{C_k}$	6×6	Hydrostatic stiffness matrix of the kth submodule
$\boldsymbol{u_k}$	6×1	6-DOF displacement of the kth submodule expressed as $(x_k, y_k, z_k, \alpha_k, \beta_k, \gamma_k)^T$
$\boldsymbol{a_{kj}}$	6×6	Added mass matrix of the kth submodule induced by the motion of the jth submodule
$\boldsymbol{b_{kj}}$	6×6	Radiation damping matrix of the kth submodule induced by the motion of the jth submodule
$\boldsymbol{u_j}$	6×1	6-DOF displacement of the jth submodule expressed as $(x_j, y_j, z_j, \alpha_j, \beta_j, \gamma_j)^T$
$\boldsymbol{f_{exk}}$	6×1	Wave excitation force (or moment) of the kth submodule

The Laboratory in Hydrodynamics, Energetics & Atmospheric Environment (LHEEA) of L'École centrale de Nantes developed the world's first open-source Boundary Element Method (BEM) code, NEMOH (LHEEA Cetrale Nantes, 2017). NEMOH had been fundamentally developed to obtain the frequency-domain coefficients of a hydrodynamic problem. It was further developed to accommodate multiple bodies. It is commonly used in academic circles, especially in the field of wave energy.

When compared to the widely used commercial alternative WAMIT, NEMOH was shown to have good overall agreement for many cases providing added-mass, radiation damping and excitation force coefficients; poor results only occur when using thin elements (Penalba, et al., 2017). NEMOH utilizes established boundary element methods. A small summary of the core assumptions of NEMOH can be found in Appendix A, most of which are common among BEM diffraction software (LHEEA Centrale Nantes, 2017).

Figure 3.2 shows the setup created to utilise NEMOH for this study. The NEMOH outputs used for this study are added mass matrix, radiation damping matrix and wave excitation force (or moment). Formats and matrix dimensions are as shown in Table 3.1.

The inputs required by NEMOH are the geometry mesh describing the body and environmental parameters describing the fluid field. The open-source platform Salome is used to create the mesh. Unfortunately, NEMOHs native mesh format cannot be outputted directly and must be converted using a script written in linux bash provided by one of the creators of NEMOH. This requires moving files around folder trees, which is done using an OCTAVE script. This meshing, converting and copying must be repeated for each body. The same OCTAVE script is used to create a NEMOH input file containing all the required file references and environmental data before moving it to the right folder. Finally, a windows executable .bat file created to run the NEMOH preProcessor, solver and postprocessor in the right order is run from the same OCTAVE script. This OCTAVE script allows the entire process of running NEMOH to be automatic and controlled from one location.

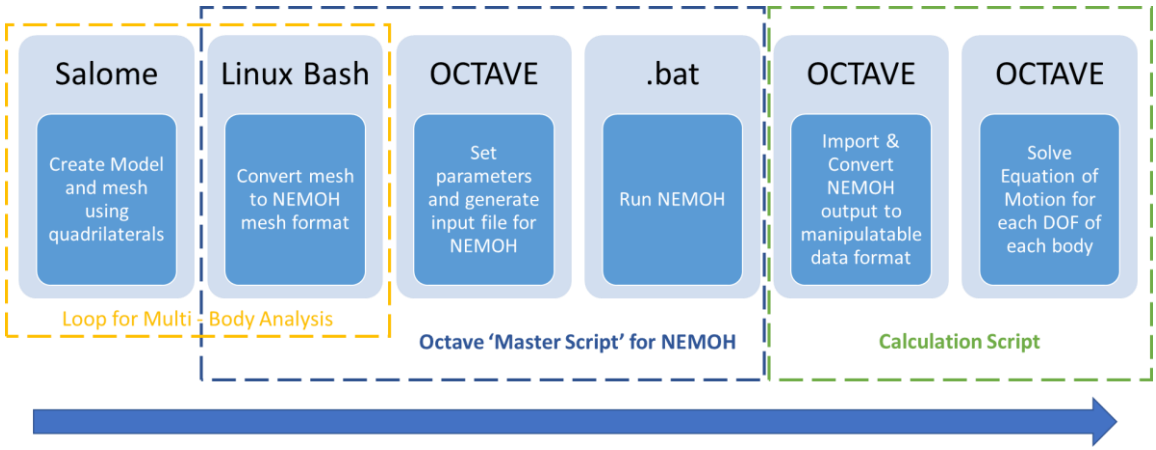

Figure 3.2: NEMOH Setup

Calculation Script

The NEMOH outputs are the then converted into a human readable and easily manipulable format using a different OCTAVE calculation script. The other EOM inputs, mass and hydrostatic stiffness matrices, that must be manually inputted as shown in Figure 3.1 are programmatically inputted along with the various structural and environmental variables needed to calculate them for each given body.

Once all the required pre-requisites are met, an equation of motion (EOM) is setup as shown in Figure 3.1. Each body and degree of freedom has a corresponding equation. All the equations are arranged into a large matrix equation and then solved using OCTAVES built-in solver for the u_k and u_j values. These values can be easily scaled by wave amplitude into RAOs, the aim of the thesis. It should be noted that by default, NEMOH computes these values for a wave amplitude of 1 m. This is reflected in the values for the wave excitation force f_{exk}. Therefore, once the EOM is solved using NEMOH output values, u_k and u_j are already scaled for 1 m waves. Note that radiated waves are calculated in all directions.

4. Verification and Validation

4.1. Single Body Verification

The primary verification model is a rectangular box of dimensions $L = 1.6$ m, $B = 0.2$ m, $T = 0.1$ m with the centre of gravity at the undisturbed free surface. The box has zero forward speed and is in deep water conditions. Head waves are introduced at 0°, thereby hitting the structure on its short side first. A frequency range of $0.05 - 30$ rad/s has been used for the analysis. All analysis was done in six degrees of freedom.

Figure 4.1 shows a representation mesh of the verification model. The panels on the undisturbed free surface plane should be noted. Its impact will be discussed later in this section.

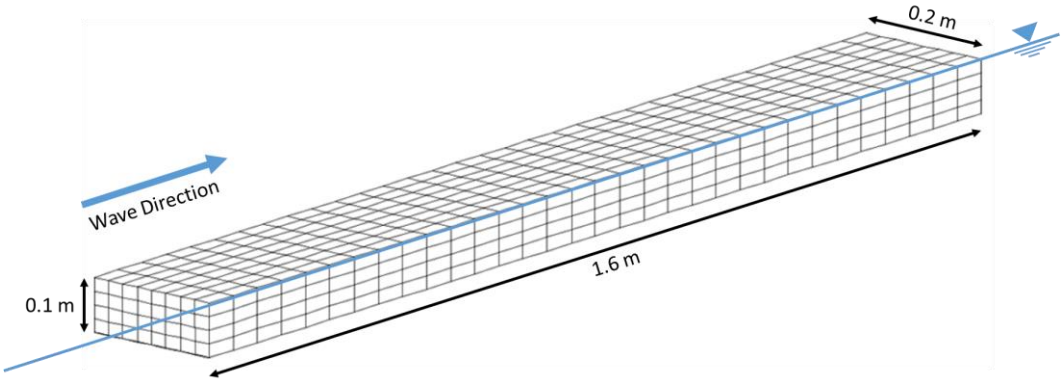

Figure 4.1: Primary Verification Model Mesh

Added Mass & Radiation Damping Coefficients

The added mass and radiation damping coefficients outputted by NEMOH were compared against results from DELFRAC, another diffraction software, and (Du, et al., 2012). Note that (Du, et al., 2012) only provide data for sway and heave. Therefore, those two degrees of freedom have been shown in Figure 4.2 so that two sources may be used for verification.

In their study on the impact of lids (panels at undisturbed free surface shown in Figure 4.1) on computations using diffraction software, (Du, et al., 2012) used the primary verification model. They showed that the mathematical basis for diffraction code leads to the irregular frequencies among the higher frequencies and that the most practical solution to removing them is by modelling a lid on the mesh. Both NEMOH and DELFRAC display irregular frequencies (large deviations from a smooth curve) at the same frequencies. Unfortunately, NEMOH cannot solve for meshes with lids and outputs no data when asked to do so. Inputting such a mesh results in no solution output. Therefore, meshes without lids were used for both NEMOH and DELFRAC analysis.

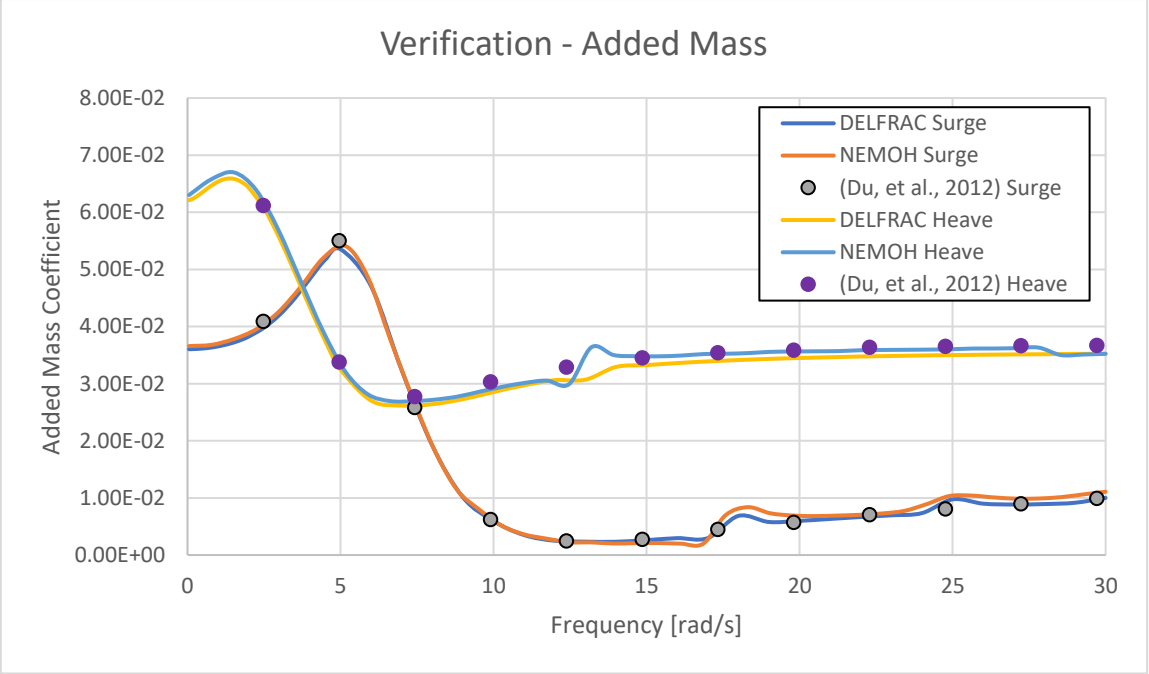

Figure 4.2: Verification Results for Added Mass Coefficients

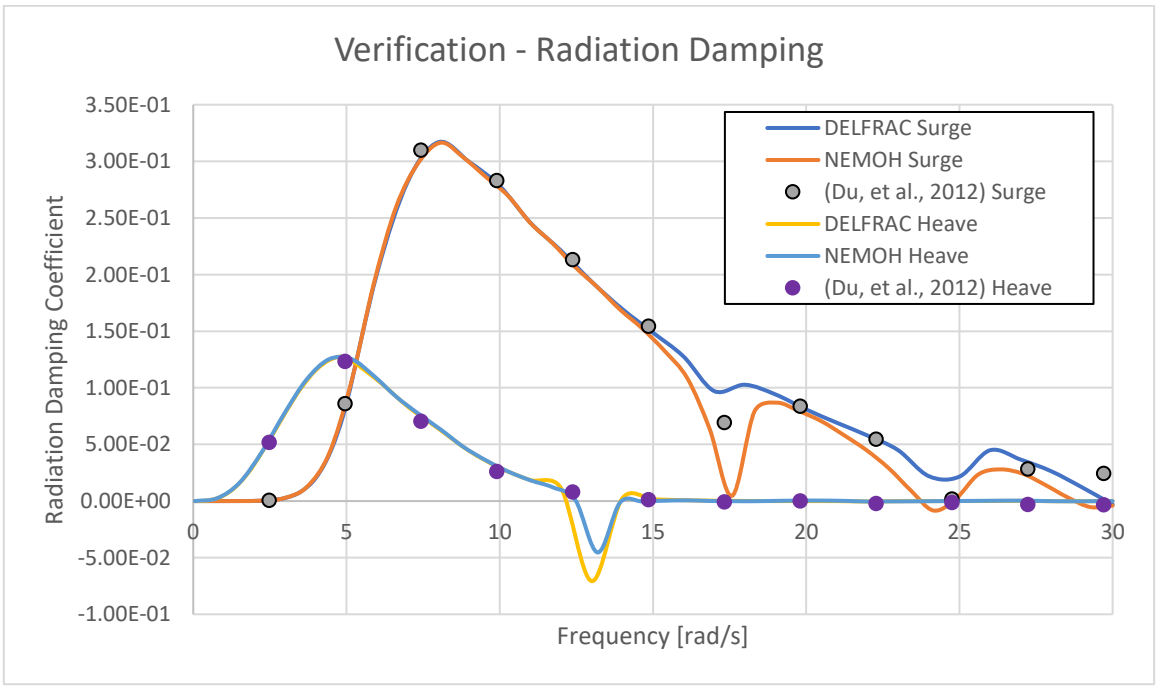

Figure 4.3: Verification Results for Radiation Damping Coefficients

In general, the plots in Figure 4.2 and Figure 4.3 show good agreement between NEMOH, DELFRAC and (Du, et al., 2012). At the irregular frequencies, both NEMOH and DELFRAC show large errors. These irregular frequencies can be seen at around 17 rad/s and 25 rad/s for sway and 13 rad/s for heave. Due to the constraints of the tools, these irregular frequencies will have to be recognized and worked around for all cases.

The frequencies at which such irregularities occur can be estimated using equation 4.1 where g is the gravitational acceleration, T is draft and γ can be calculated using equation 4.2 (Inglis & Price, 1981).

$$\omega_{\alpha\beta} = \sqrt{g\gamma T \coth(\gamma)}$$
$$\alpha = 1,2,3,\ldots;\beta = 1,2,3,\ldots \quad (4.1)$$

$$\gamma^2 = \left(\frac{\alpha\pi}{L}\right)^2 + \left(\frac{\beta\pi}{B}\right)^2 \quad (4.2)$$

The lowest frequency at which irregularities arise correspond to ω_{11} which is 13 rad/s for the verification model. This matches well with the results shown in Figure 4.2 and Figure 4.3.

Wave excitation force

The magnitude of the wave excitation forces outputted by NEMOH were compared against results from DELFRAC for the verification model. The data is taken from the same runs used for the verification of added mass and radiation damping coefficients. Both DELFRAC and NEMOH output the wave excitation force with two values, amplitude and phase. The amplitudes are shown in Figure 4.4 and their units are in kN/m and kN for translational and rotational degrees of freedom respectively. This means that these values have already been normalized with respect to wave amplitude. The verification results for the magnitude of wave excitation force is shown in Figure 4.4. The NEMOH and DELFRAC results show good agreement for both the amplitude and phase.

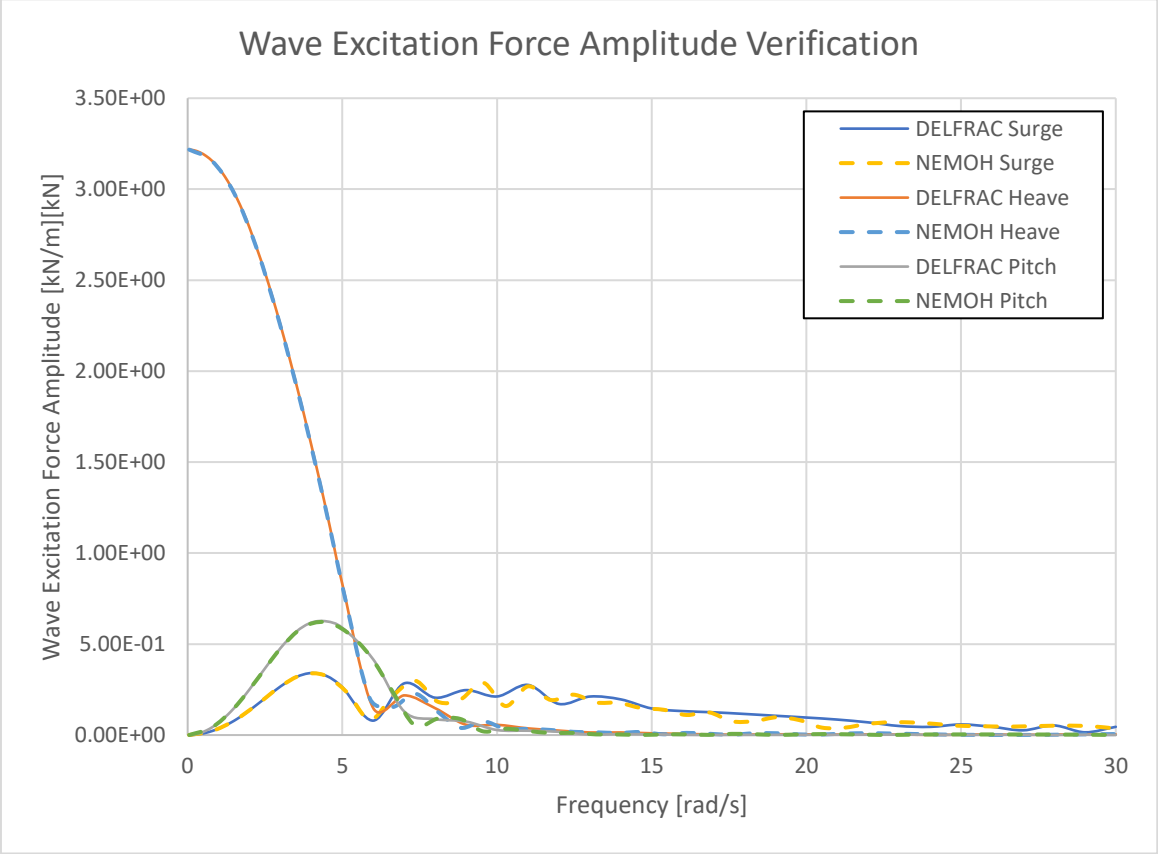

Figure 4.4: Verification Results for Amplitude of Wave Excitation Force

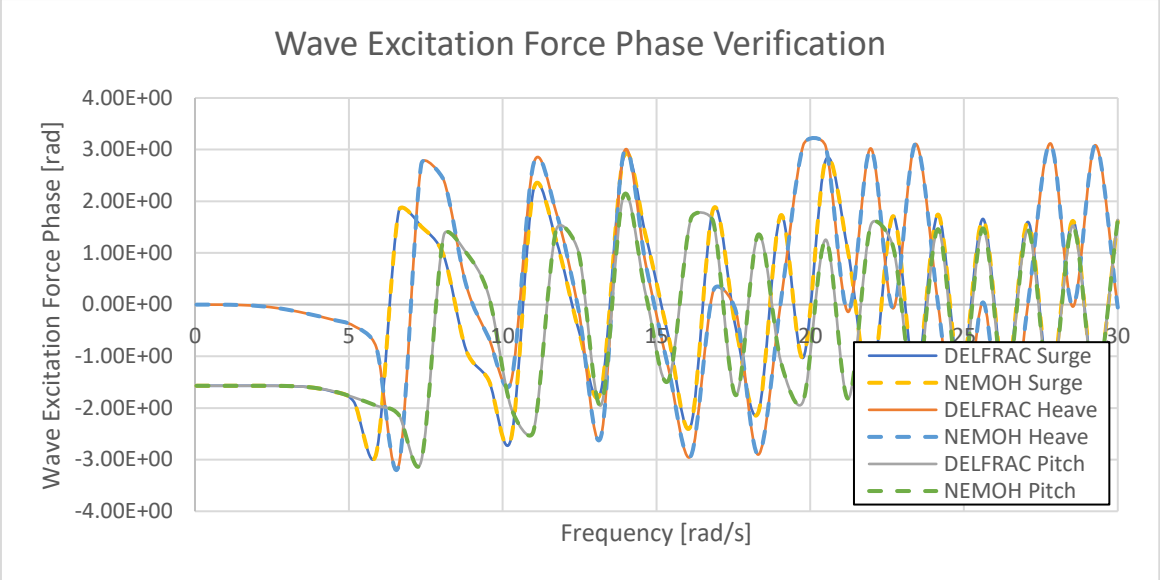

Figure 4.5: Verification Results for Phase of Wave Excitation

Mesh Convergence Test

A mesh convergence was study done on the verification model. The added mass and radiation damping in sway and heave, labelled as A22, A33, B22 and B33 respectively, are shown for analysis done on meshes with different number of panels in Figure 4.6. There is a clear convergence to a final solution past the datapoint at 470 panels for all four coefficients being shown. The 470 panels mesh corresponds to approximately square panels with sides of $0.04m$ each. This results in a panel to body ratio of 40: 1. The panel to wavelength ratio that gave converged values in tested cases ranged from 250: 1 to 2: 1 as frequency changed.

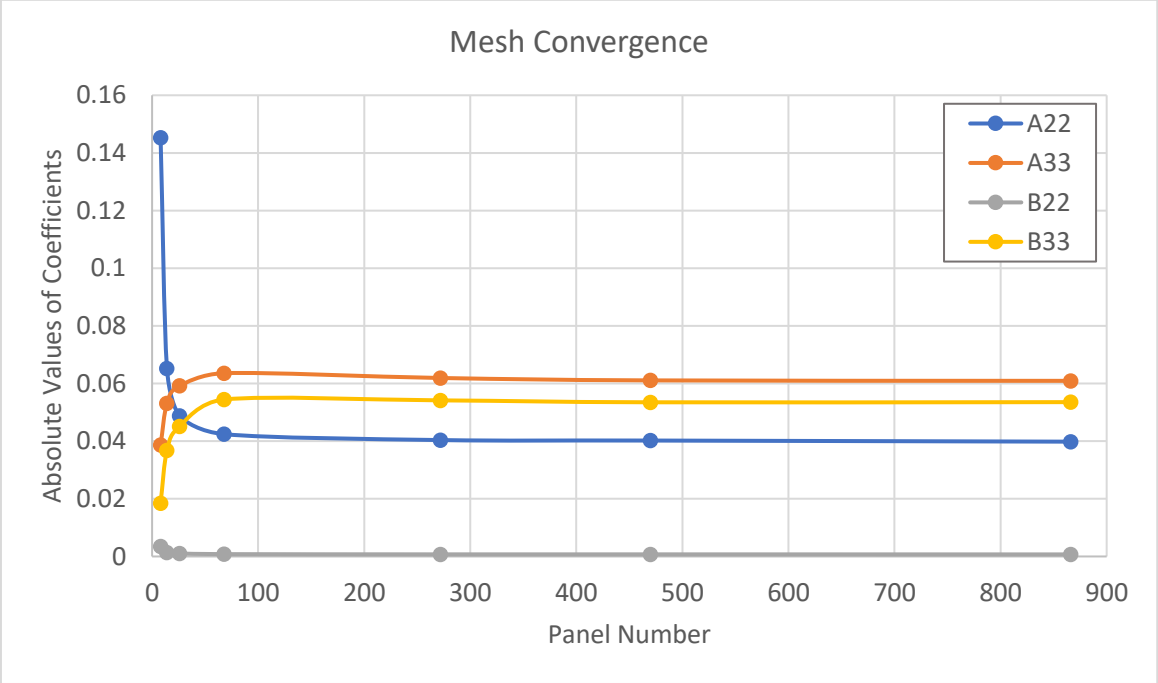

Figure 4.6: Mesh Convergence Plot

4.2. Multi-Body Validation

In order to validate the multi-body capabilities of NEMOH and verify the manually programmed mass and hydrostatic stiffness matrices, a case from (Feng & Bai, 2017) was used. The case, used as validation for their journal paper as well, contains two identical bodies of $L = 2$ m, $B = 1$ m, $T = 0.3$ m, which are placed at 90° angles, close to each other as shown in Figure 4.7. Note that the global and local coordinate systems are different for Body 2. Both bodies are analysed in six degrees of freedom. A mesh with 1520 panels for each body was used. The mesh had a panel to body ratio of 40: 1 and panel to wavelength ratio ranging from 100: 1 to 15: 1 as frequencies changed.

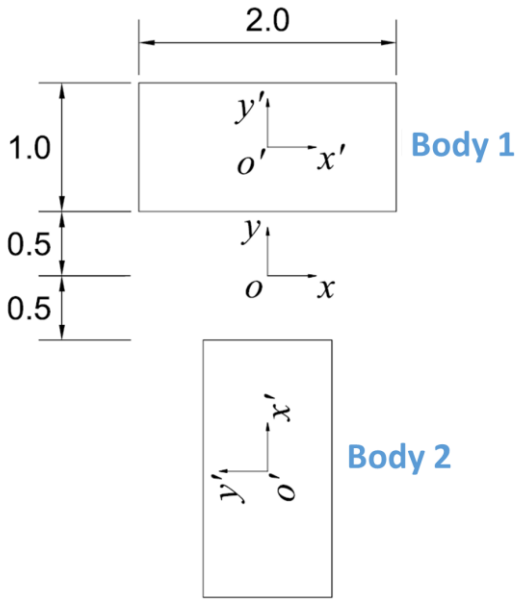

Figure 4.7: Validation Model Layout

(Feng & Bai, 2017) utilized the commercialized linear frequency-domain software package HydroStar® to validate their nonlinear decomposition model in the framework of potential flow using this model case. The same HydroStar® results are being used to validate the multi-body hydrodynamic coupling in this thesis.

The validation results for the two bodies are shown in Figure 4.8 and Figure 4.9. The results from combined tool used in this thesis matches those from HydroStar® very well. Comparing the response amplitude operators (RAOs) of the two bodies shows the hydrodynamic coupling working. The layout of the two barges in the fluid domain should result in a coupling between the roll of Body 1 and the pitch of Body 2. A similar coupling should exist between the sway of Body 1 and the surge of Body 2. Both these hydrodynamic couplings are clearly shown through the shared resonance frequencies between the coupled motions. The relevant resonance frequencies are at 6.2 rad/s and through a matching trend approaching 5 rad/s. Since the smallest irregular frequency corresponding to bodies of these dimensions is 6.63 rad/s, the resonance frequency calculations are not impacted by such an error.

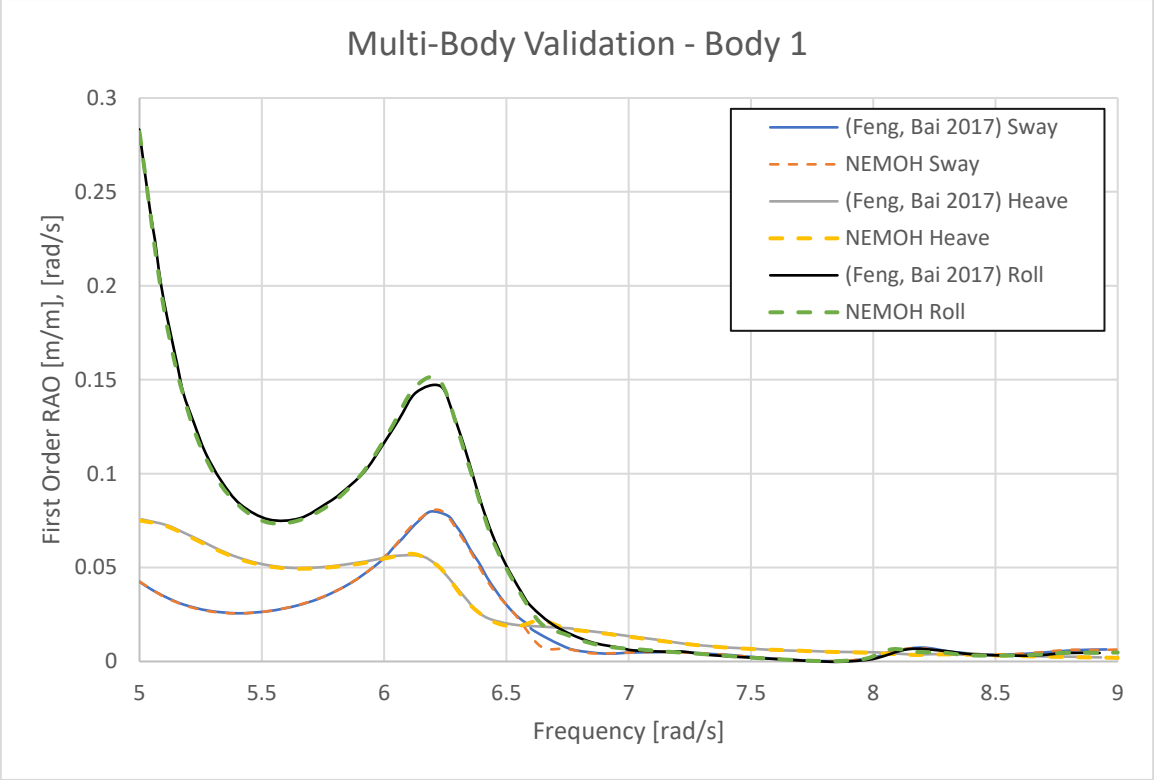

Figure 4.8: Validation Results for Body 1

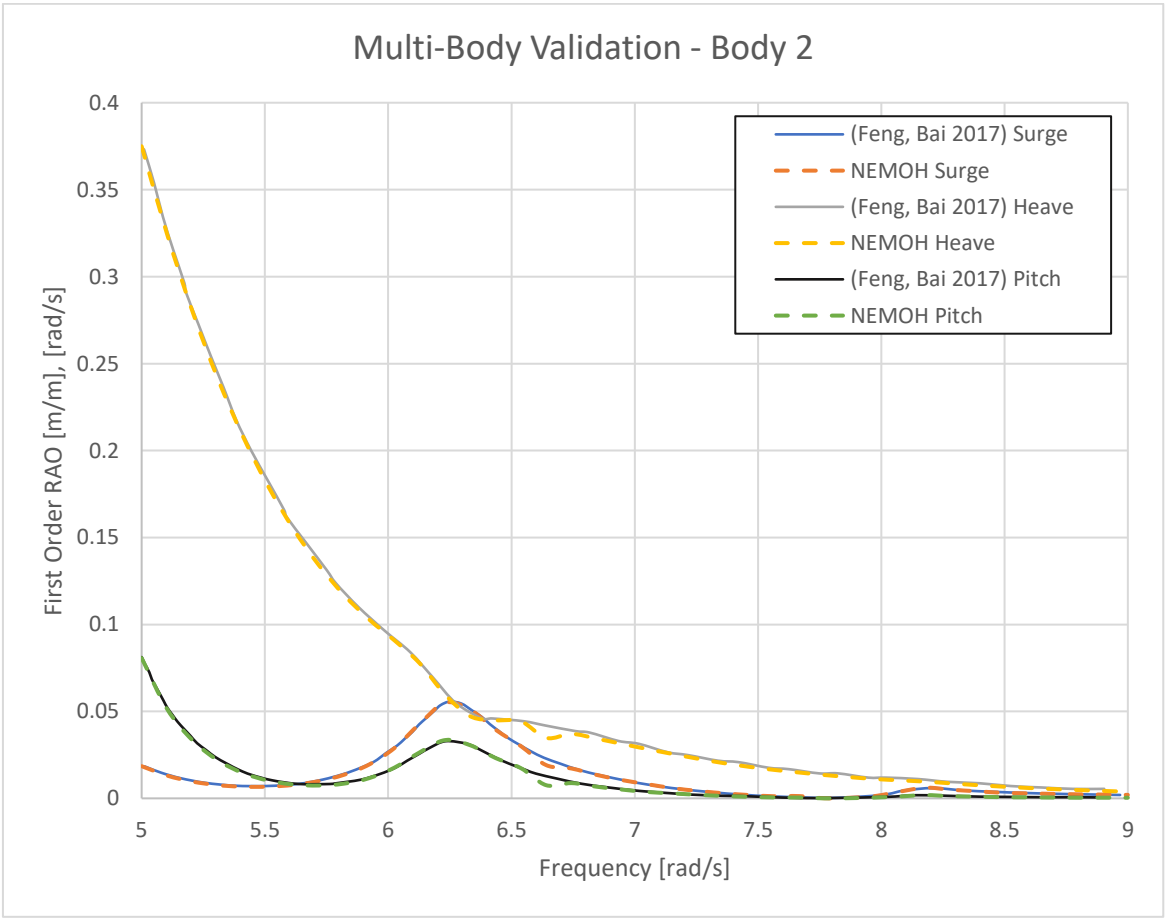

Figure 4.9: Validation Results for Body 2

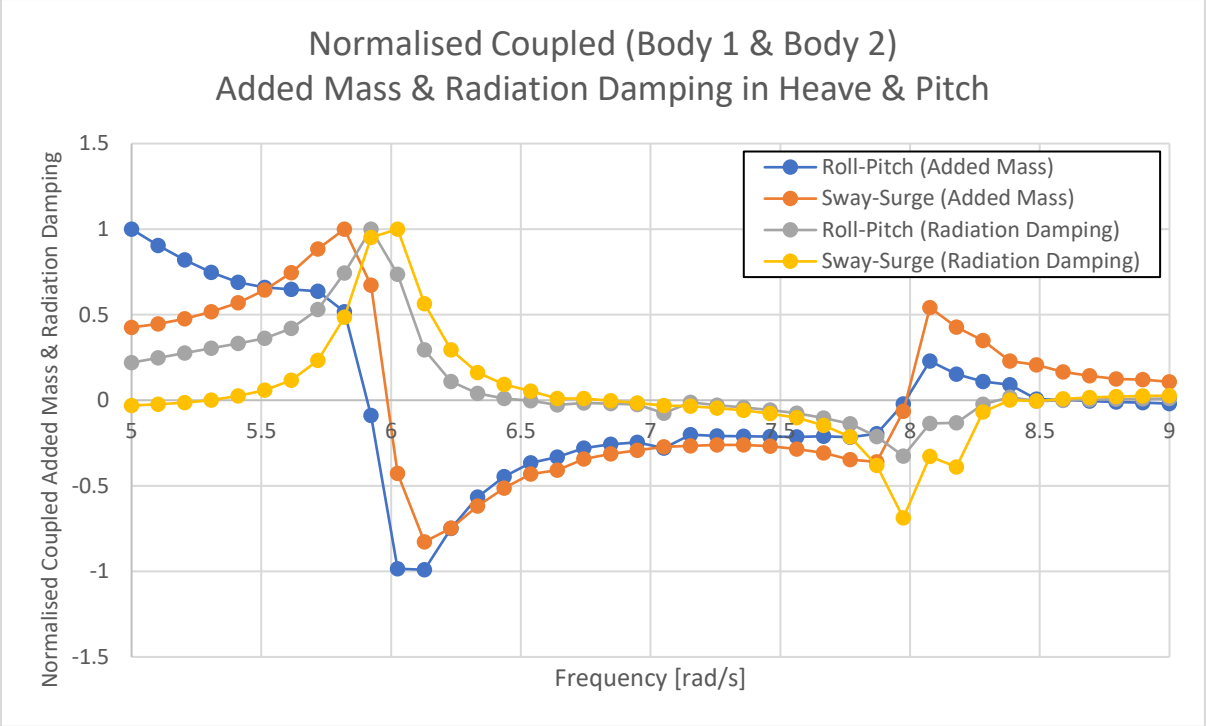

Figure 4.10: Normalised Coupled (Body 1 & Body 2) Added Mass & Radiation Damping in Heave & Pitch

The hydrodynamic coupling can also be seen by looking at the coupled hydrodynamic coefficients between the two bodies. The normalised Roll-Pitch & Sway-Surge coupled added mass and radiation damping are shown in Figure 4.10. The natural frequencies identified for the system in Figure 4.8 and Figure 4.9 are in the same vicinity as the peaks shown here. This shows that there is indeed hydrodynamic coupling between the two bodies.

5. Case Study

The case study looks at wave frequency motions of hydrodynamically coupled individual floating bodies representing a potential configuration for floating cities with a breakwater placed upstream of the platforms. The method, as described in Chapter 3 above, explains some of the choices made towards simplification on the technical side. Cases with varying parameters in breakwater width and distance are tested and there are results shown here. These cases should be tested for the frequency corresponding to the spectral peak of the wave energy at the chosen location.

5.1. Case Study Model

Ideally, the chosen site would be in a bay or lake like Ijsselmeer in these early days for floating cities. Due to inability to acquire wave data for such a location, a location in the North Sea had to be chosen. This means that much larger structures are needed to avoid resonance in the most common sea states in-situ than this thesis would like to consider.

To ensure that the platforms/breakwater motions are minimised, the platform/breakwater must be designed such that its natural frequency in all degrees of freedom avoid the frequency associated with the wave spectrum peak at the location it is intended to be placed in. This ensures that the most common sea state does not cause resonant response in the platforms/breakwater. As shown in Figure 5.1, the wave spectrum peak frequency at the site chosen in the exclusive economic zone of the Netherlands in the North Sea is 0.75 rad/s. Note that all case study models are analysed for $0°$ wave direction, or head waves, unless specified otherwise and included a breakwater with 10 platforms downstream of it.

The chosen location is an intermediate water depth site of 22 m depth at wave frequencies of 0.75 rad/s. This corresponds to a wavelength (λ) of 97.4 m. Since $97.4\ \text{m} < 627\ \text{m}$, the structure behaves rigidly and hydroelasticity can be safely neglected. Structures with length to wavelength ratios greater than 0.35, or in this case side lengths greater than 34 m, will have wave transmission coefficient (k_t) < 0.5 (Wang, et al., 2010). Gap resonance can occur if the gap length, parallel to wave crest, matches $(n \times \lambda)/2$ as discussed before (Elchahal, et al., 2009). However, since only head waves are being considered, the likelihood of it happening is reduced since only some diffracted waves can travel perpendicular to wave direction.

The gap between the platforms is chosen at a reasonable value of 20 m. This gap size allows platforms to be interconnected with reasonably sized bridges, and the gap used as canals. The horizontal axis begins at the breakwater for all analysis. Note that the orientations of the three dimensions are shown in a schematic in Figure 5.2 where L is the length, i.e. the side parallel to wave direction, B is the width, the side parallel to wave crest and T is the draft.

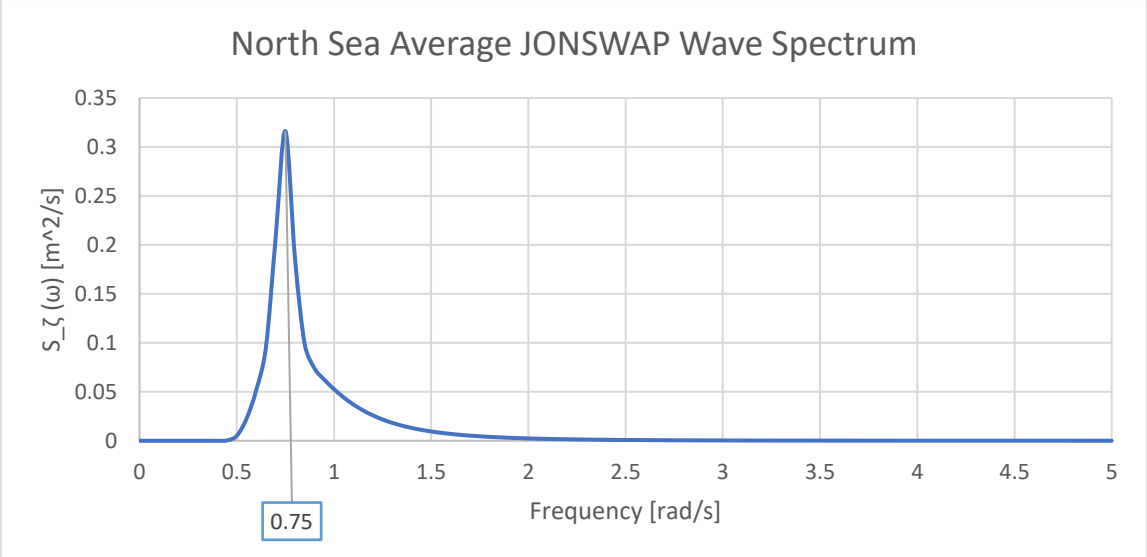

Figure 5.1: North Sea Average Wave Spectrum (Spectrum Peak at 0.75 rad/s)

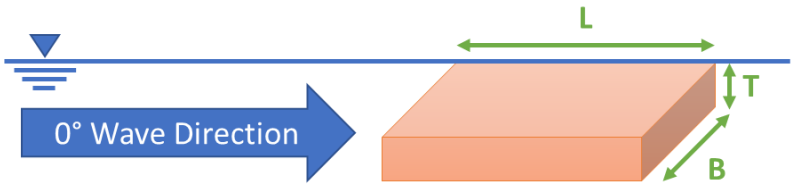

Figure 5.2: Schematic of orientation of dimensions

Platform Dimensions

A simple square shape with $B = L$ is chosen to reduce the number of variable parameters in the structure. The natural frequencies for heave and pitch/roll (same due to square shape) can be calculated using simplified analytical equations for a range of side length and draft values using the equations below (Summey, et al., 1978) where ω_n is the natural frequency in rad/s, C_k is the hydrostatic stiffness, M is the mass moment inertia, a is the added mass and x refers to the degree of freedom being analysed.

$$\omega_{n_x} = \sqrt{\frac{C_{k_x}}{M_x + a_x}} \tag{5.1}$$

The hydrostatic stiffness for the relevant degrees of freedom can be calculated using the equations below. $C_{k_{33}}$ refers to heave and $C_{k_{44,55}}$ refers to roll, pitch. In the equations, ρ is the density of water, g is the gravitational acceleration, A_{wl} is the waterplane area, ∇ is the submerged volume, z_{COG} is the vertical location of the centre of gravity, z_{COB} is the vertical location of the centre of buoyancy, and L is the length of the structure parallel to the wave direction.

$$C_{k_{33}} = \rho g A_{wl}$$
$$C_{k_{44,55}} = \rho g \left(\nabla(-z_{COG} + z_{COB}) + \frac{1}{12} L^4 \right) \tag{5.2}$$

The added mass for the relevant degrees of freedom can be calculated using the equations below. a_{33} refers to heave and $a_{44,55}$ refers to roll, pitch. In the equation for $a_{44,55}$, k_{rot} has a value of 0.41 for square structures (Gracey, 1941).

$$a_{33} = \left(\frac{1}{\sqrt{1 + \frac{A_{wl}}{L^2}}} \right) \frac{\pi \rho L^5}{4}$$

$$a_{44,55} = k_{rot} \frac{\pi \rho L^5}{48} \tag{5.3}$$

The ranges for length and draft were selected based on rough estimations of what reasonable values for such a structure should be. The centre of gravity is placed at the volumetric centre of the platform to reduce complexity, placing it at still water level. This was done for both the platforms and the breakwater.

The natural heave frequencies for all combinations of side length and draft were two orders of magnitude smaller than the spectral peak value and therefore do not contribute to the platform dimensioning. The pitch/roll natural frequencies, however, were a lot closer as shown in Table 5.1. It is clear that the side length has a much larger impact than the draft.

Table 5.1: Estimated natural frequency in roll/pitch for varying side lengths and draft

Natural Frequency [rad/s] in Roll/Pitch of platforms with side length [m] in rows and draft [m] in columns					
Side Length \ Draft	**1**	**2**	**3**	**4**	**5**
50	0.781	0.784	0.789	0.795	0.803
60	0.713	0.715	0.718	0.722	0.727
70	0.660	0.661	0.663	0.666	0.670
80	0.617	0.618	0.620	0.622	0.624
90	0.582	0.583	0.584	0.585	0.587
100	0.552	0.553	0.553	0.555	0.556
110	0.526	0.527	0.527	0.528	0.529
120	0.504	0.504	0.505	0.506	0.506
130	0.484	0.484	0.485	0.485	0.486
140	0.467	0.467	0.467	0.468	0.468

The platform side length is chosen to be 100 m. This allows the platform's natural frequency to avoid the wave spectrum peak frequency without making it too large. Case studies using larger platforms would not provide the data required for projects currently being investigated in this field. Considering a reasonable mass for a platform used as a city block with 100 m sides, a draft of 5 m is chosen. Further work must be done to determine the correct mass range for such a structure so that a draft can be more accurately chosen. However, that is currently beyond the scope of this thesis. It should also be noted that estimated lowest irregular frequency for a structure with such dimensions is 1.412 rad/s. Therefore, there might be certain numerical errors in diffraction results at and beyond this frequency.

Breakwater Dimensions

The floating breakwater has slightly different requirements than the platforms. Out of its three dimensions, the width (B) of the platform i.e. perpendicular to wave direction, assuming head waves, is a variable in this thesis. The k_t for a given length (L) i.e. side parallel to the wave direction, and draft (T) can be calculated using the classic formula by (Macagno, 1953) for simple box-type breakwaters. The equation is shown below where k_i is the wave number of the incident wave and h is the water depth.

$$k_t = \frac{1}{\sqrt{1 + \left[\frac{k_i L \sinh(k_i h)}{2\cosh(k_i h - k_i T)}\right]}} \tag{5.4}$$

This equation shows that the wave transmission coefficient is independent of the platform width. However, it should be noted that the wave transmission coefficient only looks at the ratio between the incoming wave energy in front of the breakwater and the wave energy behind it. The changed dimensions, and corresponding change in mass can still impact the RAOs of the platforms behind it. Furthermore, this thesis looks at a 3D problem that includes wave scattering from the breakwater, a pattern that is impacted by the width of the structure. Therefore, the research question and its variable of breakwater width is still worth investigating.

Table 5.2: Wave Transmission Coefficient for varying side lengths and draft

Wave Transmission Coefficient of width [m] in rows and draft [m] in columns analysed in-situ for peak wave spectrum frequency					
Side Length \ Draft	1	2	3	4	5
30	0.523	0.509	0.496	0.482	0.469
40	0.452	0.438	0.424	0.411	0.399
50	0.397	0.384	0.371	0.358	0.347
60	0.354	0.342	0.329	0.318	0.306
70	0.320	0.308	0.296	0.285	0.275
80	0.292	0.280	0.269	0.259	0.249
90	0.268	0.257	0.247	0.237	0.228
100	0.248	0.237	0.228	0.218	0.210
110	0.230	0.221	0.211	0.203	0.194
120	0.215	0.206	0.197	0.189	0.181
130	0.202	0.193	0.185	0.177	0.169

Table 5.2 shows the calculated k_t for varying length and draft. As expected, it is at lengths around 34 m that k_t is less than 0.5. In order to maintain commonality and a large enough k_t such that the effect in RAO is appreciable, the dimensions of the base case breakwater are chosen to be $L = 100$ m, $B = 100$ m and $T = 5$ m. The centre of gravity is placed at the volumetric centre of the platform to reduce complexity, with the vertical centre at the undisturbed level. Despite the different requirements, the k_t calculations show that the breakwater can share the same dimensions as the platforms while being functional.

5.2. Case 1: Control

Case 1 is a control case. Here the there are no variables and the base case dimensions for the breakwater are used along with the chosen dimensions for the platforms. Figure 5.3 shows a schematic of the model used for this analysis.

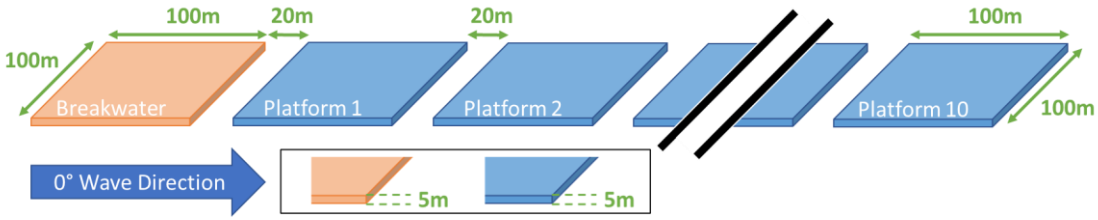

Figure 5.3: Scehmatic of model used in Case 1

Each body in the model is meshed for 1920 panels. The panel to body ratio is 40: 1 and the panel to wavelength ratio is 58: 1. These ratios are satisfactory to achieve reasonable accuracy as demonstrated in the verification and validation models. Figure 5.4 shows the heave, roll and pitch RAO at the COG of each platform at 0.75 rad/s frequency and for 0° & 90° wave directions in blue and yellow colour, respectively. Note that 0.75 rad/s is lower than the estimated lowest irregular frequency for these structures of 1.412 rad/s. The normalized horizontal length used as the horizontal axis refers to the horizontal location of COG of each platform divided by the total length from the start of the breakwater to the end of the last platform.

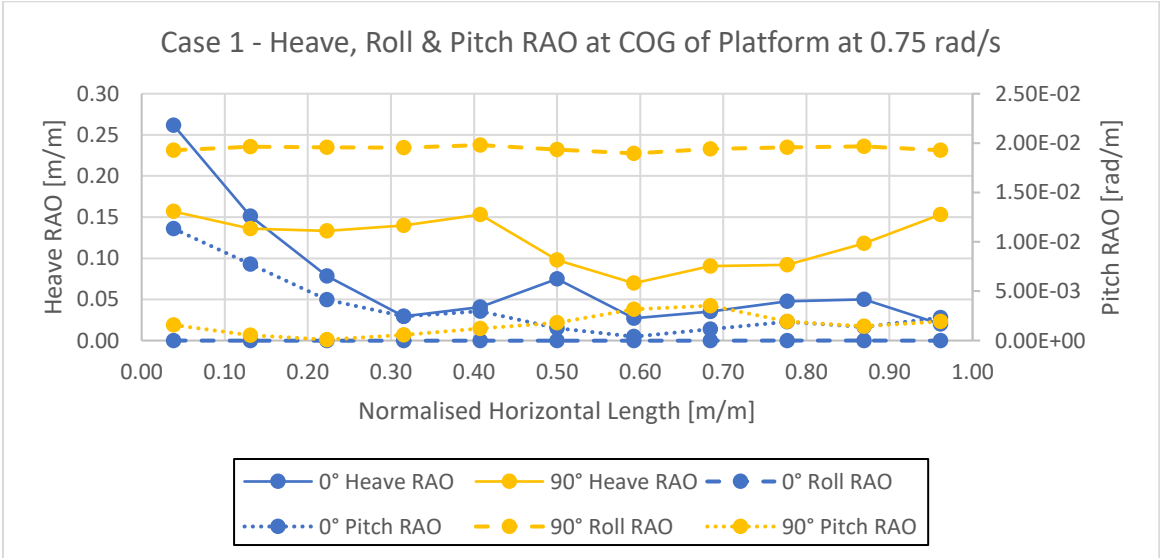

Figure 5.4: Case 1 RAO results at 0.75 rad/s. 0° wave direction (blue); 90° wave direction (yellow)

The results for Case 1 show that the breakwater only removes some of the wave energy and the platforms behind it act as breakwaters too. The difference in results between those from the 0° and 90° wave directions show that they are indeed reducing the energy of the waves for the platforms behind it. This is best seen by comparing 0° Pitch RAO and 90° Roll RAO where the 0° pitch RAO decreases drastically over the breakwater and the first three

platforms (blue dotted line) while the breakwater and all platforms move in the same way with large amplitude in roll direction when excited by waves from 90° (yellow dotted line).

5.3. Case 2: Changing gap between breakwater and platforms

Case 2 introduces one variable. Here, the base case dimensions for the breakwater are used again along with the chosen dimensions for the platforms. Only the gap between the breakwater and the next platform is changed in increments of 20 m. The gap between the platforms remains the same at 20 m. Figure 5.5 shows a schematic of the model used for this analysis. The variable parameter has been labelled as x.

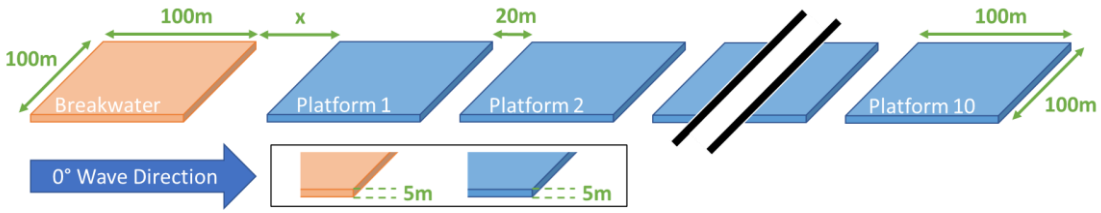

Figure 5.5: Schematic of model used in Case 2

The mesh resolutions and wave frequency remain the same as in Case 1 at 1920 panels and 0.75 rad/s respectively. Note that 0.75 rad/s is lower than the estimated lowest irregular frequency for these structures of 1.412 rad/s. Only the breakwater has been moved in space. Figure 5.6 and Figure 5.7 show the heave and pitch RAOs respectively at the COG of each platform. Due to the changing gap, the horizontal location of the COG of each platform shifts too. This shift can be seen by the vertical misalignment between the data points for different gap sizes for all the platforms.

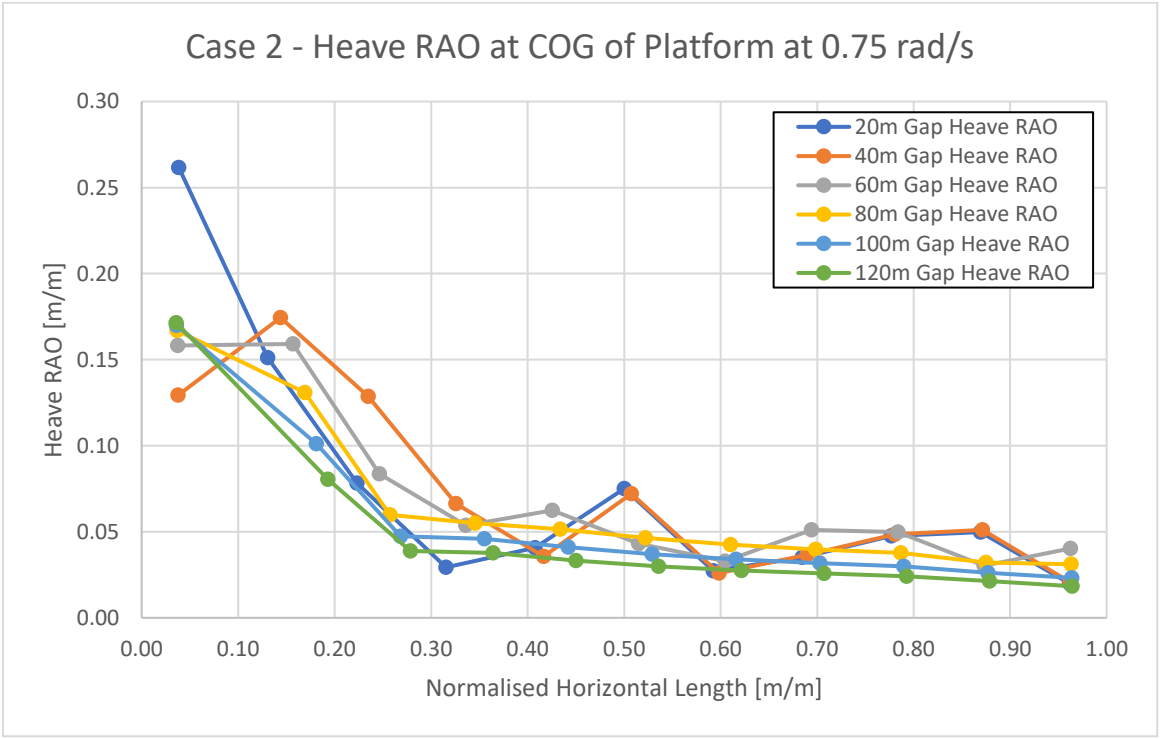

Figure 5.6: Case 2 Heave RAO Results at 0.75 rad/s

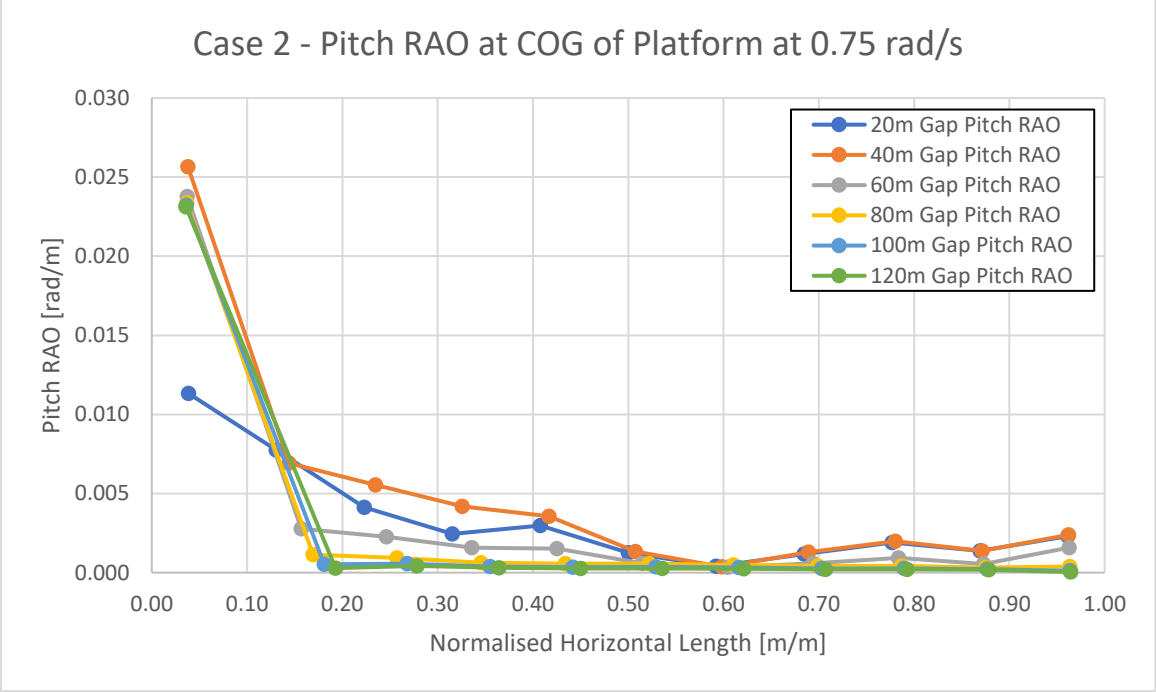

Figure 5.7: Case 2 Pitch RAO Results at 0.75 rad/s

The results for Case 2 show that as the distance between the breakwater and the first platform increases both the heave and pitch RAOs show larger decreases for the platforms behind them. The pitch RAOs show this trend quite clearly such that the pitch is minimised from the first platform (second data point) itself. This effect begins to be significant at and beyond 60 m gap. Further increases in gap size show diminishing returns. This means that increasing the gap size results in smaller and smaller reductions in RAO.

As seen in Case 1, the breakwater alone is not enough to completely absorb all the wave energy. The platforms right behind it still act as breakwaters themselves. This trend is shown quite clearly in the Heave RAOs. It takes about 2 platforms at large gap sizes to minimize the heave RAOs. This effect begins to be significant at and beyond 80 m gap. Further increase in gap size show diminishing results where there is a proportionately smaller decrease in RAO for a further increase in gap size.

Further investigation into the hydrodynamic coupling coefficients for heave and pitch, shown in Figure 5.8, implies that the hydrodynamic coupling increases as the gap increases. It should be noted that there is a difference in trend before and after the 40 m gap size. Hydrodynamic coupling effects are clearly playing a part in the improved RAO results as gap sizes increase, but further studies will need to be done to determine the exact physical phenomenon.

Considering the functionality of the platforms as city blocks, minimizing the pitch motion is more important than the heave motion because they correspond to large local heave at the edges of the structure. In actual projects, the breakwater will have to surround the structure on more than one direction. Therefore, the larger the gap size, the longer/larger the breakwaters will have to be. As such, a 80 m gap is chosen as the recommended gap size for platforms and breakwaters such those used in this case study.

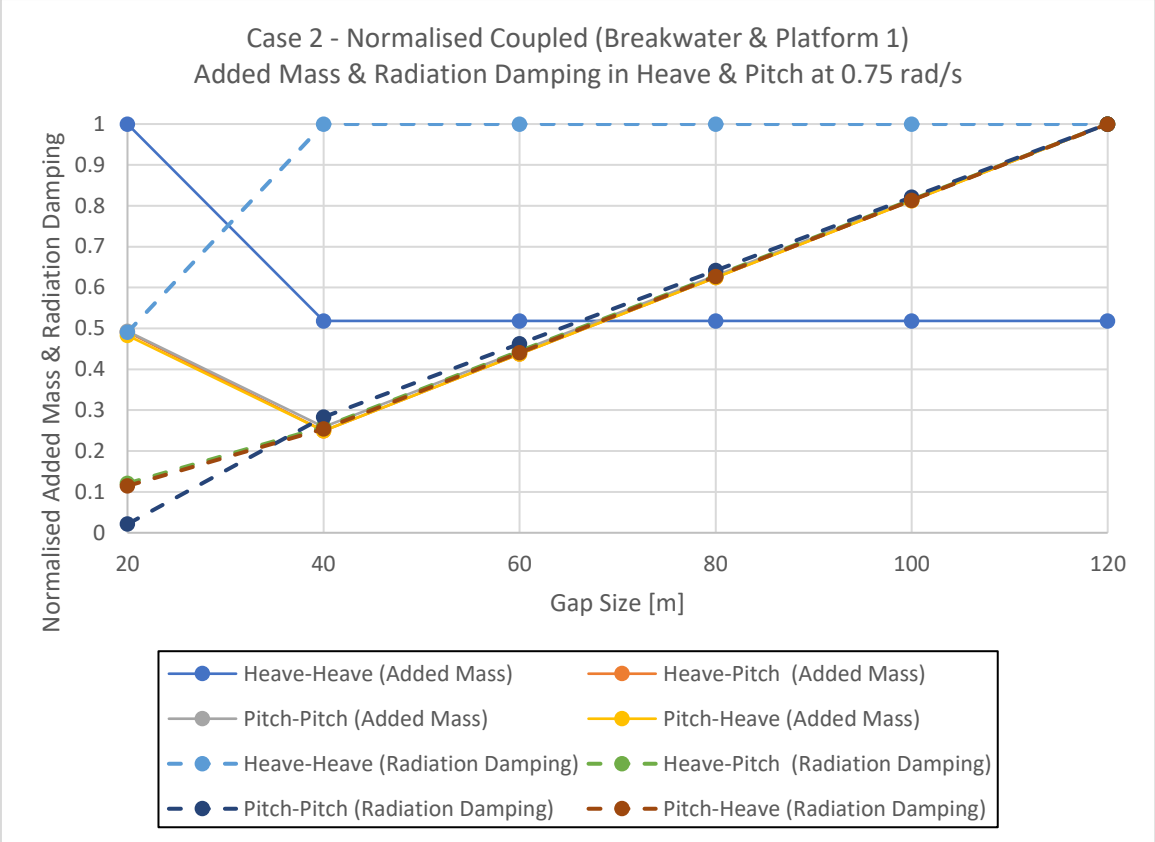

Figure 5.8: Normalised Coupled (Breakwater & Platform 1) Added Mass & Radiation Damping in Heave & Pitch at 0.75 rad/s

5.4. Case 3: Changing width of the breakwater

In Case 3, the chosen dimensions for the platforms are used. Only the width of the breakwater is changed to 200 m and 300 m. The gaps between the breakwater and platforms that are analysed are 20 m and 80 m and gap between the platforms remains the same at 20 m. Figure 5.9 shows a schematic of the model used for this analysis. The variable parameter has been labelled as x.

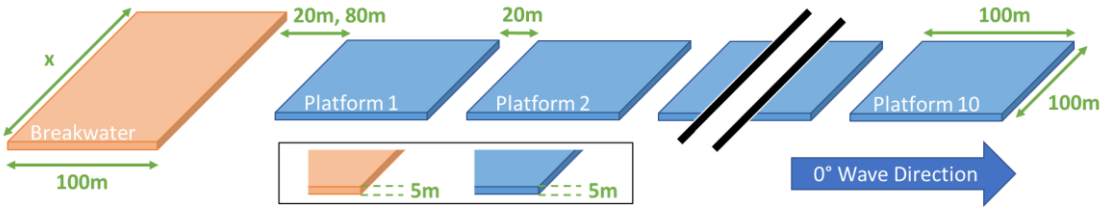

Figure 5.9: Schematic of model used in Case 3

The panel to wavelength ration remains the same as in Case 1 & 2. Only the breakwater's width is changed, resulting in higher panel count meshes for it. Figure 5.10 and Figure 5.11 show the heave and pitch RAOs respectively at the COG of each platform. All analyses are done at 0.75 rad/s. Note that 0.75 rad/s is lower than the estimated lowest irregular frequency for these structures of 1.412 rad/s. Analysis using 20m and 80 m gap sizes are

shown in orange and blue respectively. Analysis done on 100 m, 200 m and 300 m breakwater widths are shown in solid, dashed and dotted lines respectively.

The results for Case 3 show that changing the width of the breakwater has small positive impact on the heave and pitch RAO of the platforms just behind it for large gap sizes. This can be seen using the RAOs around 0.2 normalised horizontal length. However, the opposite is true for small gap sizes. Therefore, although increasing breakwater width can marginally reduce RAOs for the protected platforms, this is only true when the gap size is large.

Further investigation into the hydrodynamic coupling coefficients for heave and pitch, normalised added mass and radiation damping shown in Figure 5.12 and Figure 5.13 respectively, does not imply any clear corelation between breakwater width and hydrodynamic coupling. There is a difference in trends when comparing the data for 20 m and 80 m gap size, reinforcing the observation seen in the previous case for hydrodynamic coupling before and after the 40 m gap size. There is also a difference in trends when comparing the data for $100 - 200$ m and $200 - 300$ m breakwater width. Hydrodynamic coupling effects are clearly playing a part in the system, but the further analysis is needed.

Overall, it is clear that changing the gap has a much larger impact on the RAOs. Considering that in actual projects the breakwater will surround the platforms to protect from more wave directions, it might be feasible to marginally make the breakwater facing the primary wave direction wider. However, realistically, the impact of changing the width is too low for this to be a major breakwater design criterion. Furthermore, the added cost of doubling size for such minor impact results in a poor cost-benefit ratio. Therefore, the recommendation is to not alter the width of the structure.

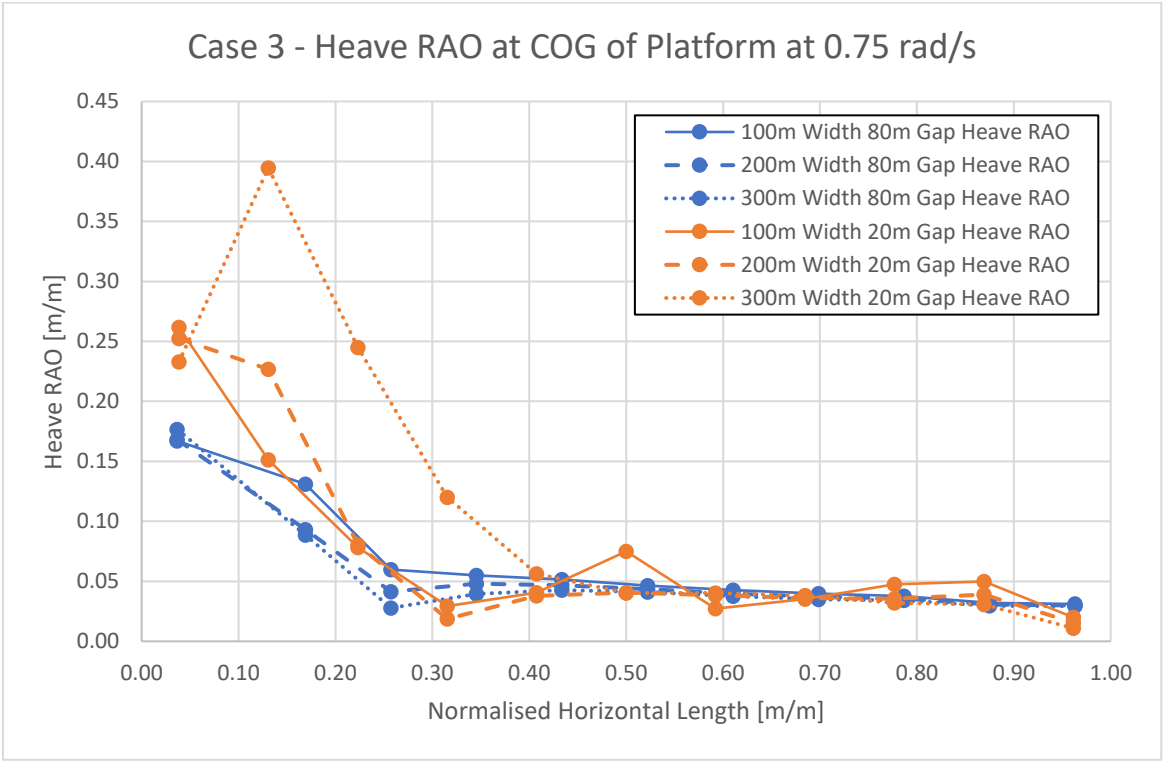

Figure 5.10: Case 3 Heave RAO Results at 0.75 rad/s. 80m gap (blue); 20m (orange)

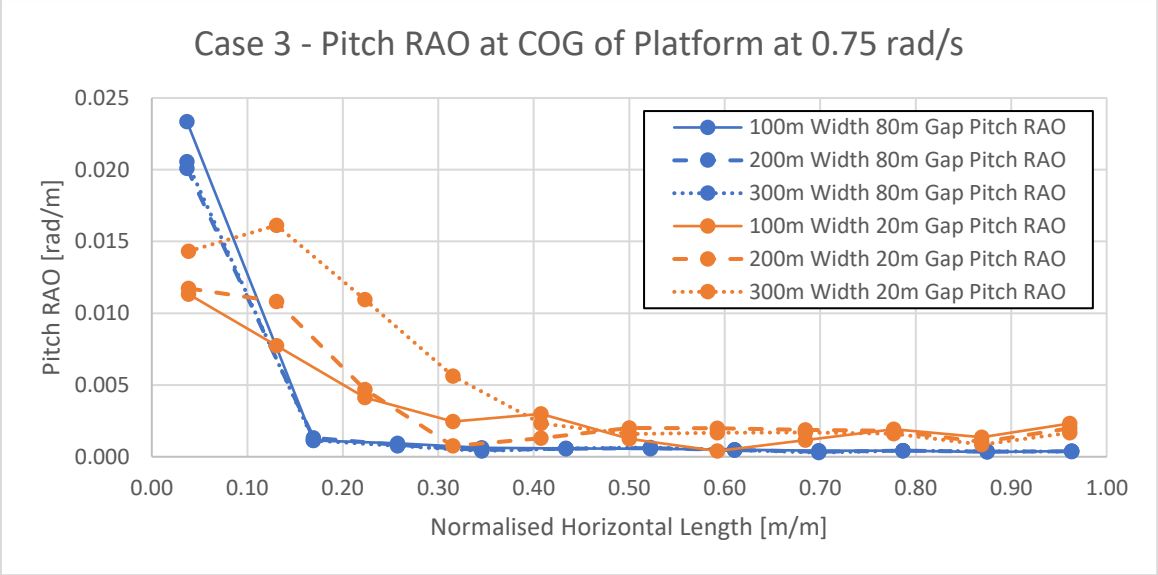

Figure 5.11: Case 3 Pitch RAO Results at 0.75 rad/s. 80m gap (blue); 20m (orange)

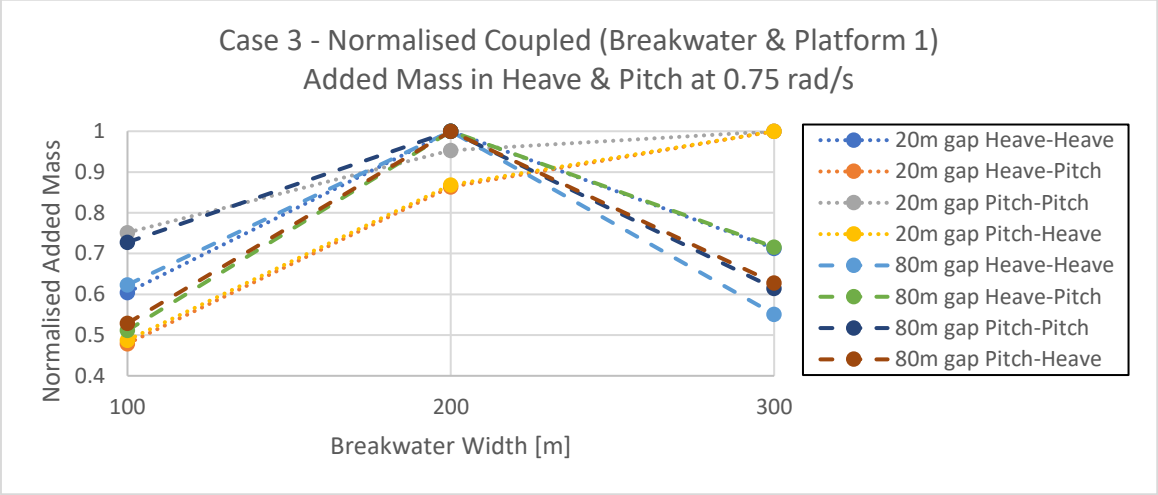

Figure 5.12: Normalised Coupled (Breakwater & Platform 1) Added Mass in Heave & Pitch at 0.75 rad/s

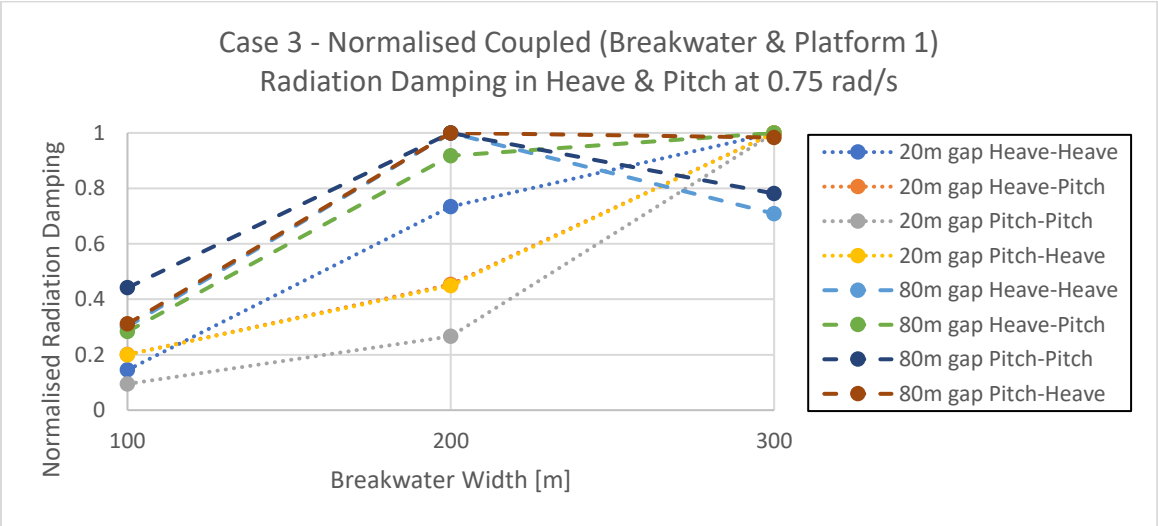

Figure 5.13: Normalised Coupled (Breakwater & Platform 1) Radiation Damping in Heave & Pitch at 0.75 rad/s

5.5. Case 4: Recommended Model

Based on the learnings from Case 2 & 3, the recommended model consists of identical breakwater and platform dimensions of $L = 100$ m, $B = 100$ m, $T = 5$ m with a gap of 80 m between the breakwater and platforms and a gap of 20 m between the platforms themselves. Figure 5.14 shows a schematic of the model used for this analysis.

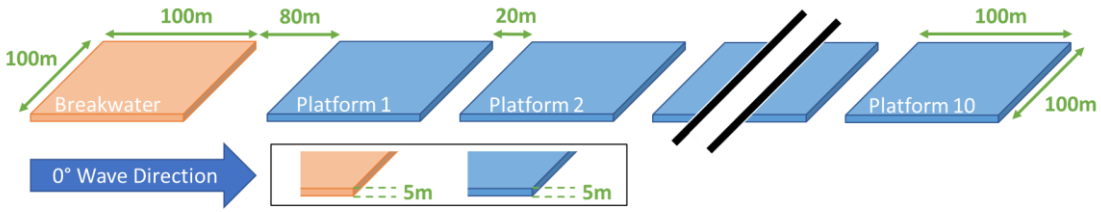

Figure 5.14: Schematic of model used in Case 4

The panel to wavelength ratio remains the same as in previous cases. This model has already been analysed in Case 2. The analysis was run for a frequency range of $0.05 - 5$ rad/s with a step size of 0.127 rad/s as shown in Figure 5.15. Figure 5.16 and Figure 5.17 show the heave and pitch RAO spectrum respectively at the COG of each platform up to 2 rad/s since there is little useful data beyond that frequency. The breakwater is plotted with a line and the platforms are indicated with individual dots. It should be noted that some results might not be accurate at frequencies greater than 1.412 rad/s due to irregular frequencies.

The bodies with the maximum RAO in heave and pitch for each analysed frequency are shown in Figure 5.18. Note that Body 1 refers to the breakwater and the platforms behind it follow ascending numbers up to Body 11 which is Platform 10, the last platform farthest away from the breakwater. The bars in blue and orange correspond to heave and pitch respectively.

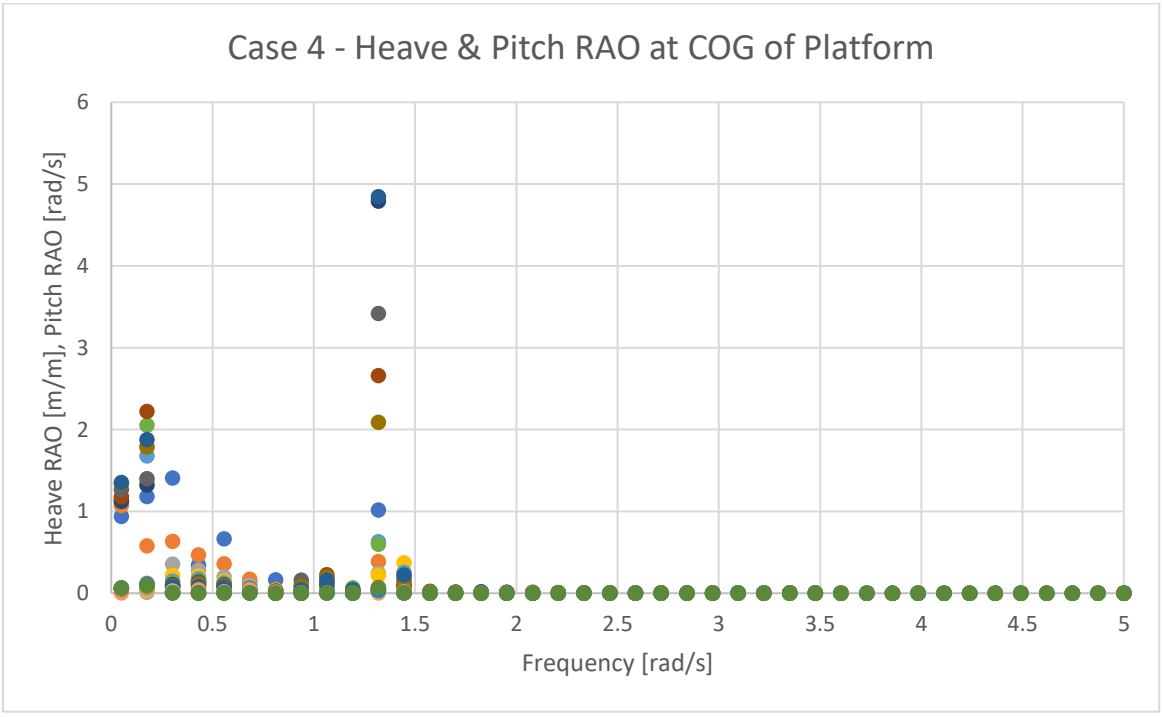

Figure 5.15: Case 4 Heave & RAO results

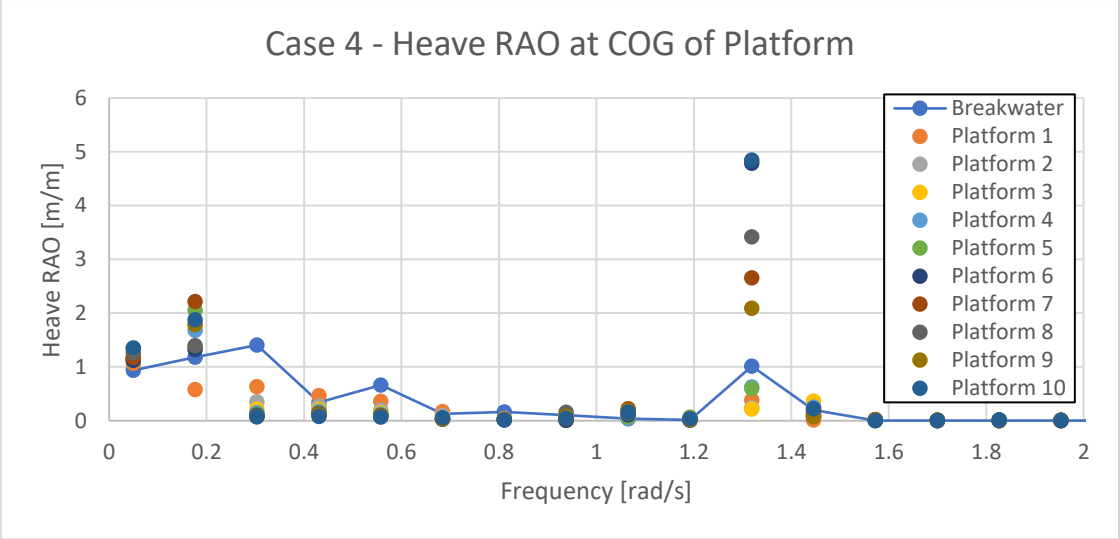

Figure 5.16: Case 4 Heave RAO results in scatter plot. Breakwater (line)

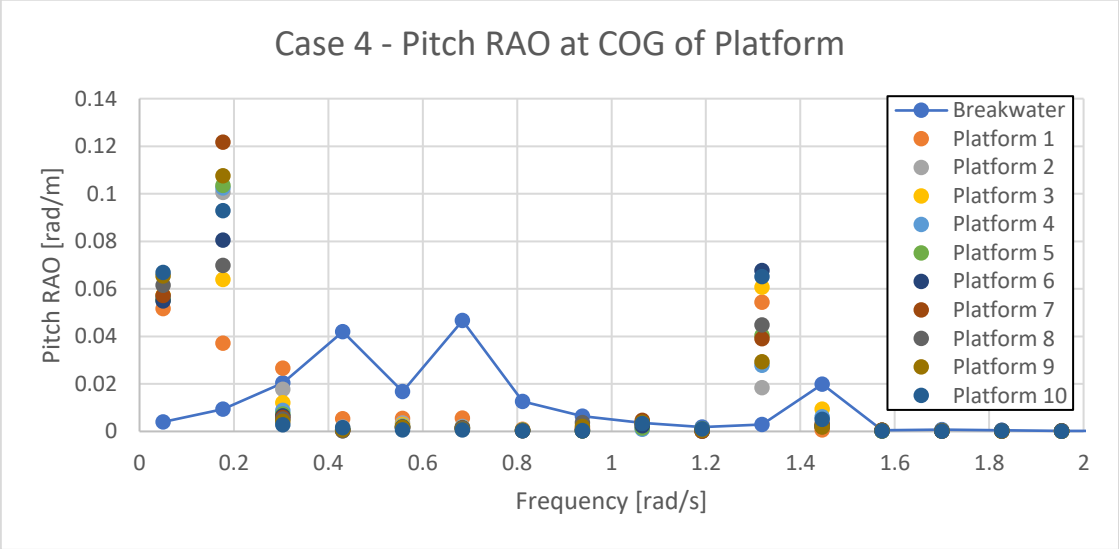

Figure 5.17: Case 4 Pitch RAO results in scatter plot. Breakwater (line)

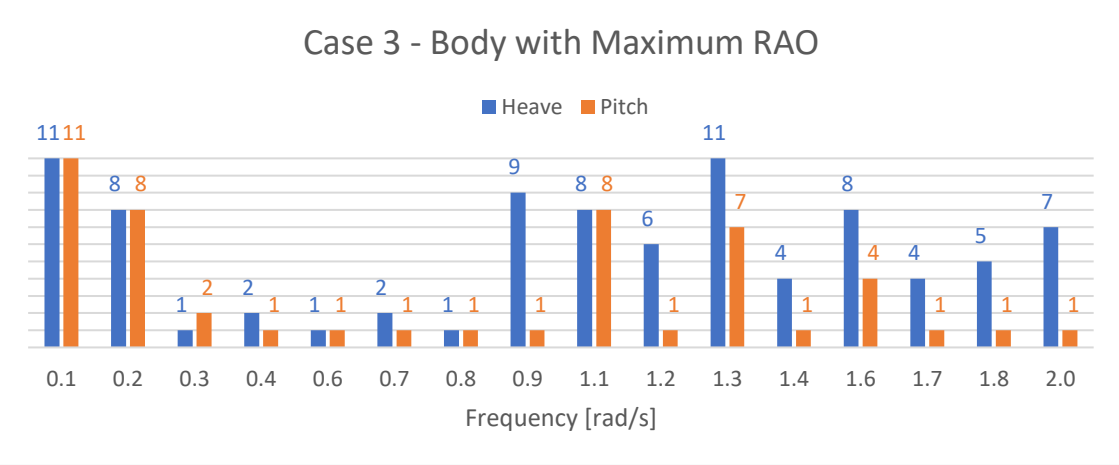

Figure 5.18: Case 3 Body with maximum RAO at frequency data point. Heave (blue); Pitch (orange)

The RAOs as a function of frequency shown in Figure 5.16 and Figure 5.17 show that the hydrodynamically coupled platforms have natural frequencies at 1.3 rad/s and 0.18 rad/s. Since the smallest irregular frequency corresponding to bodies of these dimensions is 1.412 rad/s, these natural frequency calculations are not impacted by such an error. The breakwater does not share the same natural frequencies despite being identical in dimensions to the platforms. This shows the impact of the hydrodynamic coupling between the platforms that are only 20 m apart from each other. The breakwater which was designed for 0.75 rad/s performs admirably by reflecting wave energy in most of the remaining frequency range. This can be seen in both the heave and pitch plots. Figure 5.18 shows that the breakwater is most frequently the body with the highest pitch RAO. Therefore, the breakwater has to survive larger pitch motions in order to protect the platforms behind it. Some platforms can have higher heave though.

The breakwater had been designed for a specific frequency to tailor it for the sea spectrum at a certain location. Therefore, to truly judge the success of the chosen recommended model, a response spectrum must be analysed. The response spectrum can be calculated using the equation below where S is the energy density spectrum, x refers to the DOF being analysed and ζ refers to the waves (USNA, n.d.).

$$S_x(\omega) = S_\zeta(\omega) \times RAO_x^2 \tag{5.5}$$

The analysis was run for a frequency range of $0.05 - 5$ rad/s with a step size of 0.127 rad/s . Figure 5.19 and Figure 5.20 show the heave and pitch response spectrum respectively at the COG of each platform. Note that the horizontal axis of the plots only extended up until 2 rad/s again for visual clarity. The breakwater and wave spectrum are plotted with lines and platforms with dots.

The response spectra in Figure 5.19 and Figure 5.20 show once again that the hydrodynamically coupled platforms have a natural frequency at 1.3 rad/s. The lack of wave energy at frequencies less than 0.4 rad/s results in the response there trending to zero, eliminating the impact of the natural frequency at 0.18 rad/s. Near the wave spectrum peak frequency of 0.75 rad/s, a larger response is expected. The minimal pitch response for all platforms shows the effectiveness of the breakwater. Overall, the breakwater in the recommended model performs adequately in most frequencies except at around 1.3 rad/s.

The platforms with the maximum response in heave and pitch for each analysed frequency are shown in Figure 5.21. Body numbering system remains the same as in Figure 5.18. The bars in blue and orange correspond to heave and pitch respectively. It should be noted that the last platform, Platform 10 (body 11), shows the largest heave response at 1.3 rad/s and the largest pitch response at all frequencies. One possible explanation for this might be that due to small gap size between the platform, the hydrodynamic coupling between the bodies make them behave like one large flexible body, causing the last body to whip around. Further analysis is needed to determine the cause.

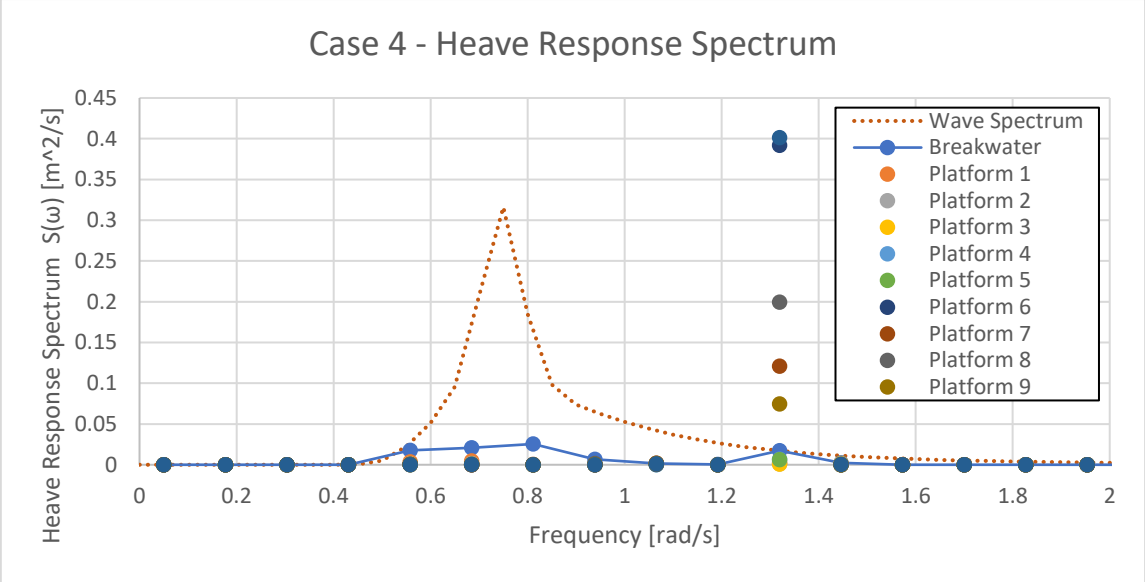

Figure 5.19: Case 4 Heave Response Spectrum results in scatter plot. Breakwater (line)

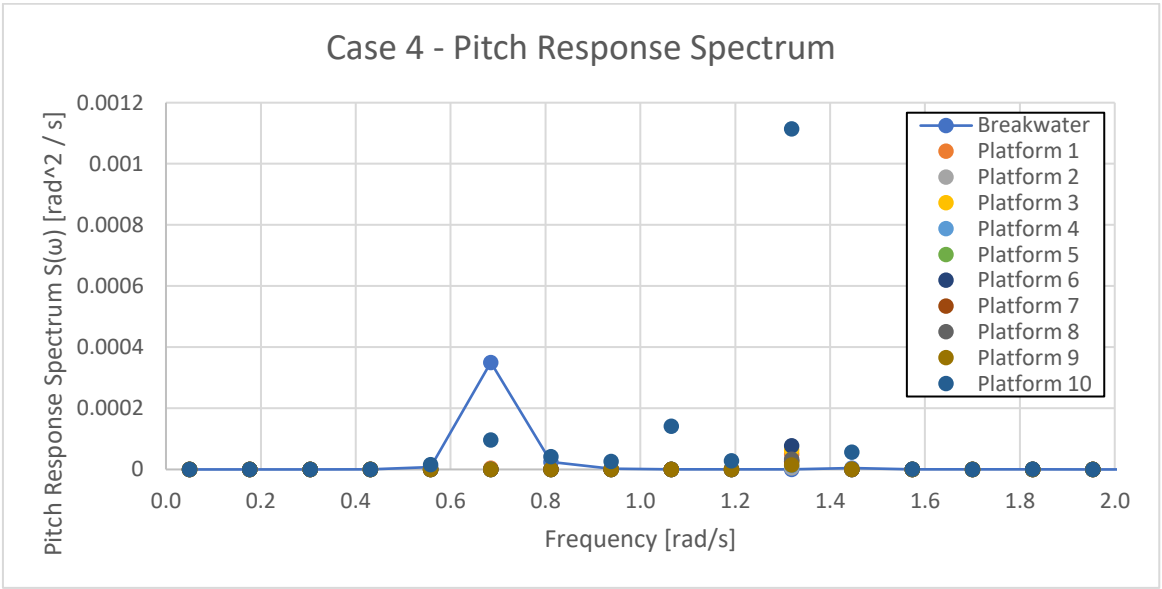

Figure 5.20: Case 4 Pitch Response Spectrum results in scatter plot. Breakwater (line)

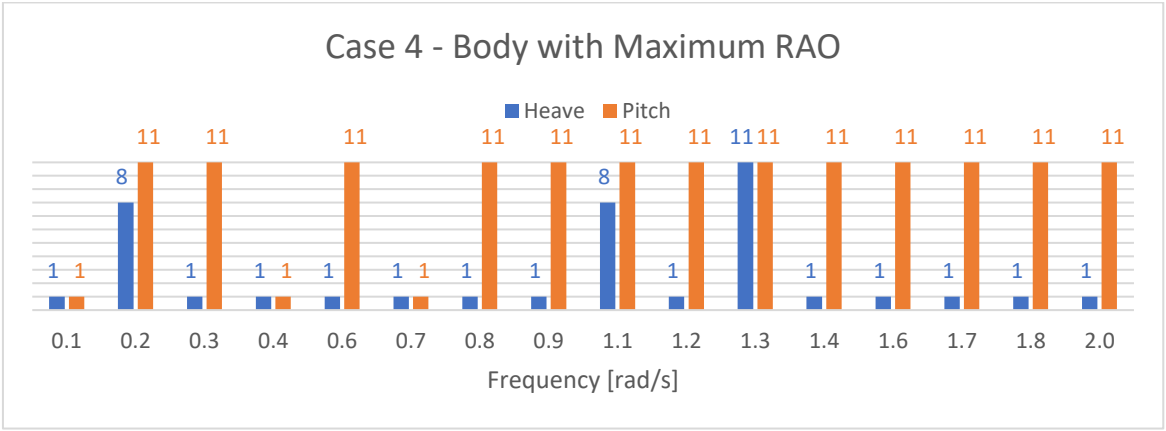

Figure 5.21: Case 4 Body with maximum response at frequency data point. Heave (blue); Pitch (orange)

5.6. Case 5: Increased Platform Gap

The results shown in the previous case studies show that the breakwater works well for the design conditions corresponding to the frequency of 0.75 rad/s. However, the results also consistently show very large RAOs and response at 0.18 rad/s and 1.3 rad/s frequencies. The latter frequency especially, falls perfectly within the range of heave motion frequency that causes motion sickness. Since these frequencies are smaller than 1.412 rad/s, irregular frequencies can be eliminated as a possible cause. This has been theorised to be the natural frequency of the hydrodynamically coupled platforms. Therefore, it should be possible to avoid the large increase in RAO and response at 0.18 rad/s and 1.3 rad/s by changing the gap between the platforms. The learnings from Case 2 are used to choose 80 m as the new gap size between platforms. Figure 5.22 shows a simplified schematic of the model.

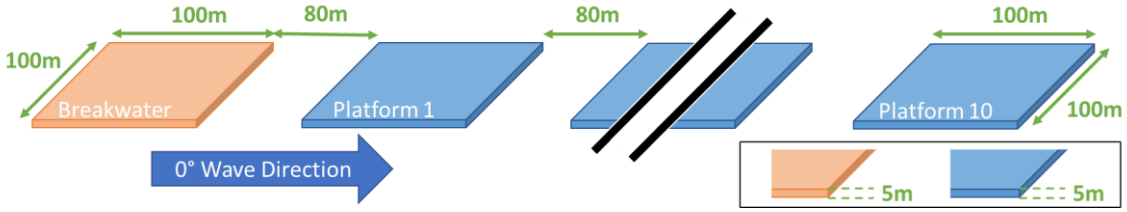

Figure 5.22: Schematic of model used in Case 5

Figure 5.23 and Figure 5.24 show the heave and pitch RAO results respectively for analysis from 0.05 – 3 rad/s with a step size of 0.1 rad/s with a higher resolution between 1.27 – 1.37 rad/s with a step size of 0.02 rad/s and an additional data point at 1.3 rad/s. The maximum platform RAOs from Case 4 are also shown using a green dotted line to better compare the results. Figure 5.25 and Figure 5.26 show the heave and pitch response spectrum respectively. The wave spectrum is also shown using an orange dotted line in the former figure. Finally, the maximum platform values from Case 4 are shown in all four figures using a green dotted line.

The results show that changing the gap between the platforms does indeed remove the natural frequencies at 0.18 rad/s and 1.3 rad/s. However, the higher frequency resolution around the natural frequency at 1.3 rad/s has also revealed another, lower RAO natural frequency at 1.37 rad/s. This peak, seen in the Heave RAO results (Figure 5.23) at around 1.37 rad/s, most probably corresponds to the breakwater coupled natural frequency since, unlike at 1.3 rad/s, the breakwater also shares this natural frequency. This breakwater coupled frequency is now the largest RAO in the frequencies analysed, although it is smaller than the coupled natural frequency previously seen at 1.3 rad/s. Pitch RAO results are satisfactory.

The RAOs and response between 0.2 rad/s and 0.9 rad/s are slightly higher for the Case 5 model when compared to the Case 4 model. This range of frequencies corresponds with larger wave energies as seen in the wave spectrum. Furthermore, the breakwater related natural frequency at 1.37 rad/s is still concerning. Overall, increasing the gap between the platforms seems to have removed the large RAO and responses corresponding to the platforms coupled natural frequency, but has had no impact on the breakwater coupled natural frequency in

heave. This latter natural frequency is still concerning since its equivalent acceleration value is larger than the 0.02 g limiting criteria for human comfort while being within the relevant frequency range for motion sickness of $0.76 - 1.57$ rad/s.

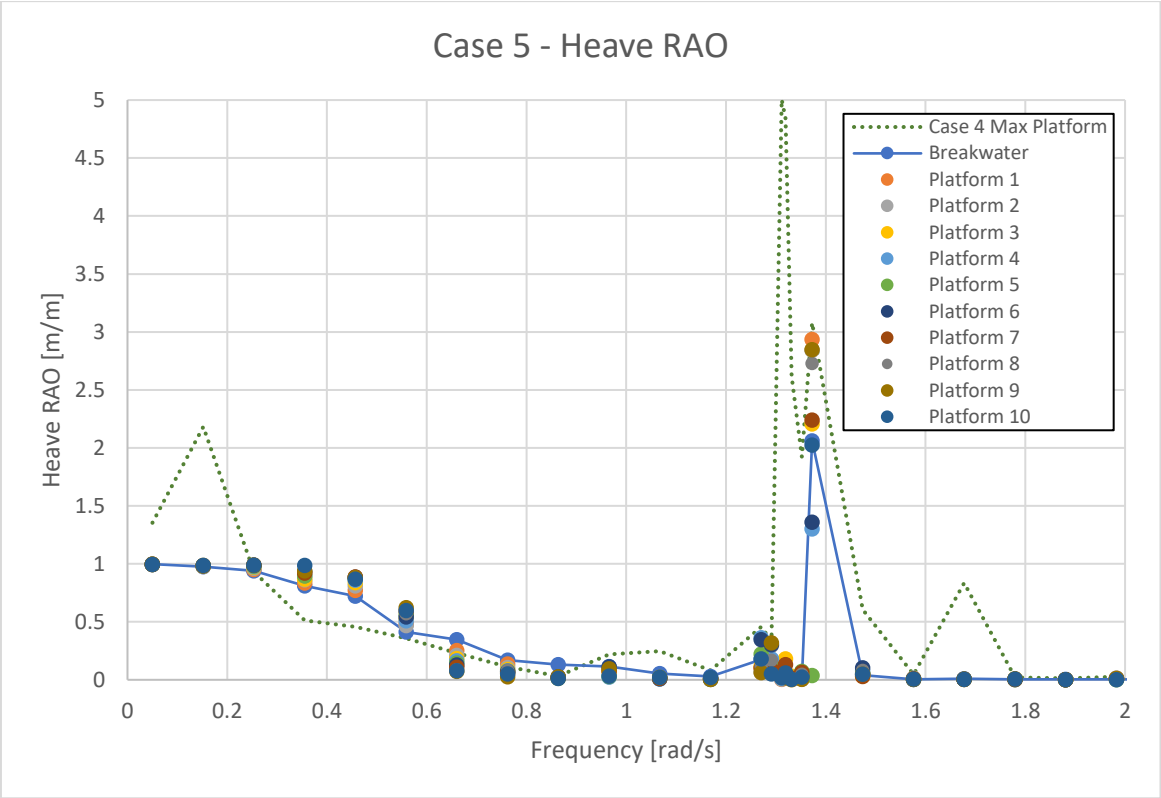

Figure 5.23: Case 5 Heave RAO results in scatter plot. Case 4 Max Platform RAO (dotted line), Breakwater (line)

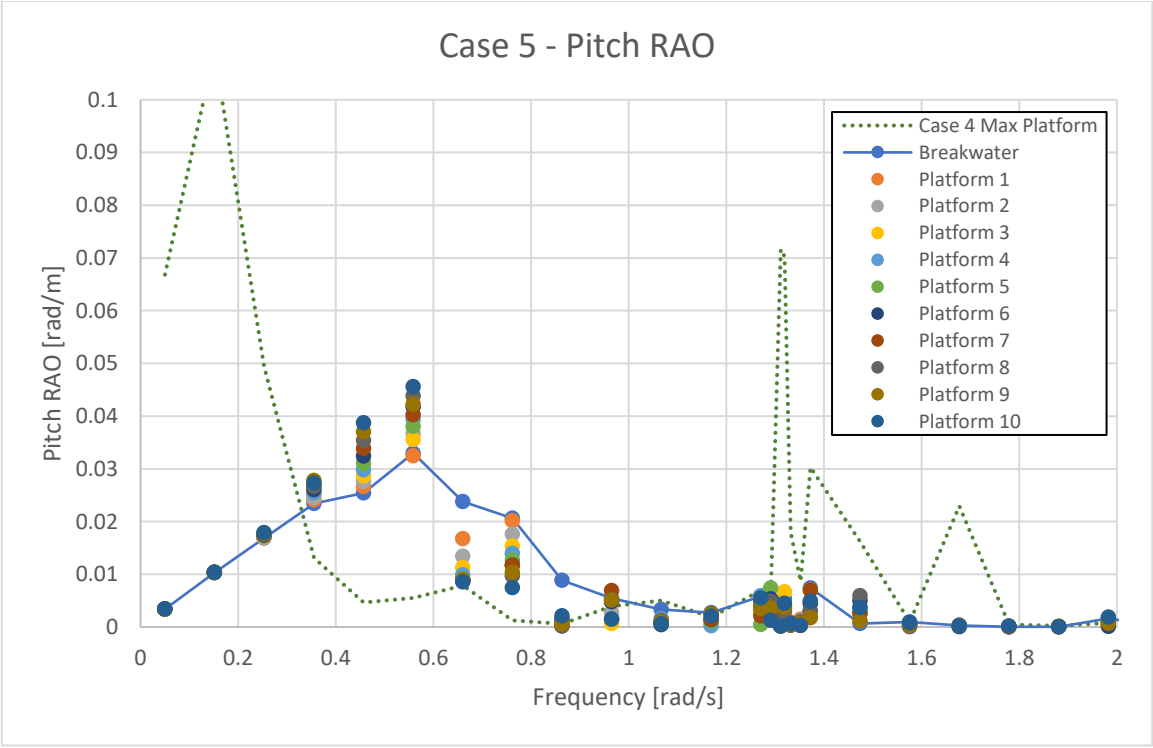

Figure 5.24: Case 5 Pitch RAO results in scatter plot. Case 4 Max Platform RAO (dotted line), Breakwater (line)

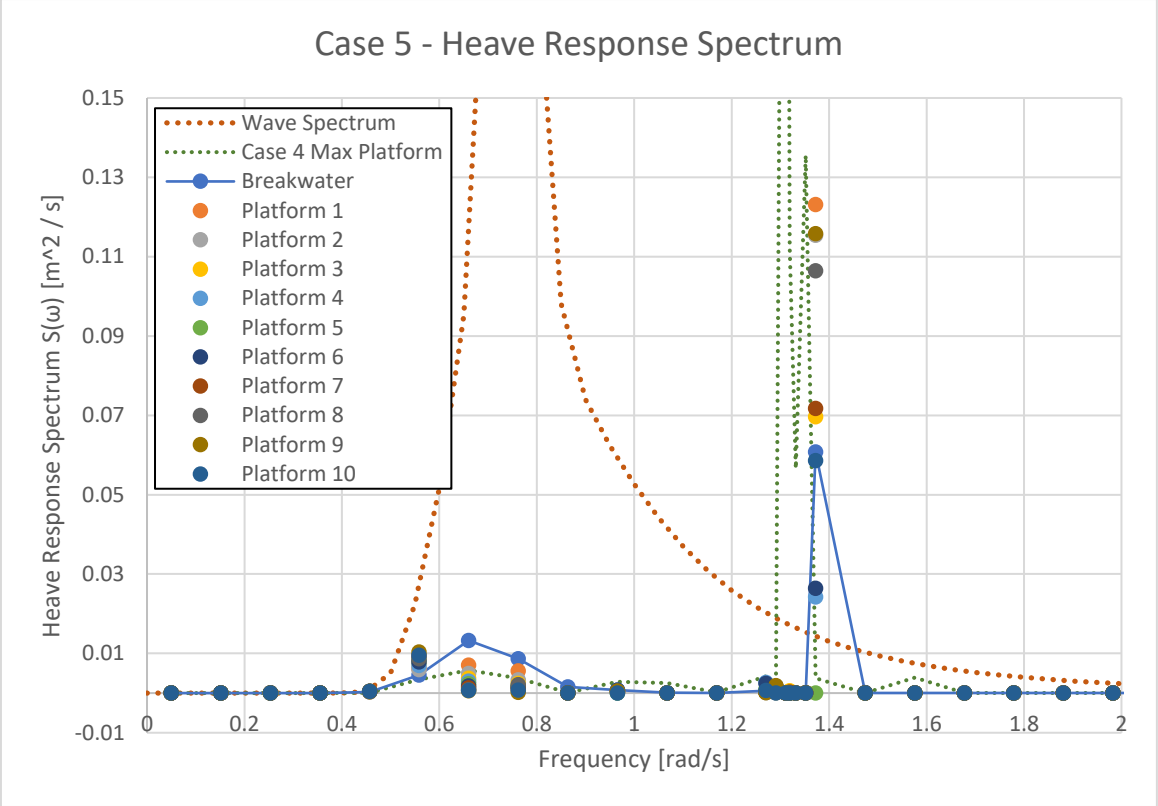

Figure 5.25: Case 5 Heave Response Spectrum results in scatter plot. Wave spectrum (orange dotted line), Case 4 Max Platform Response (green dotted line), Breakwater (blue line)

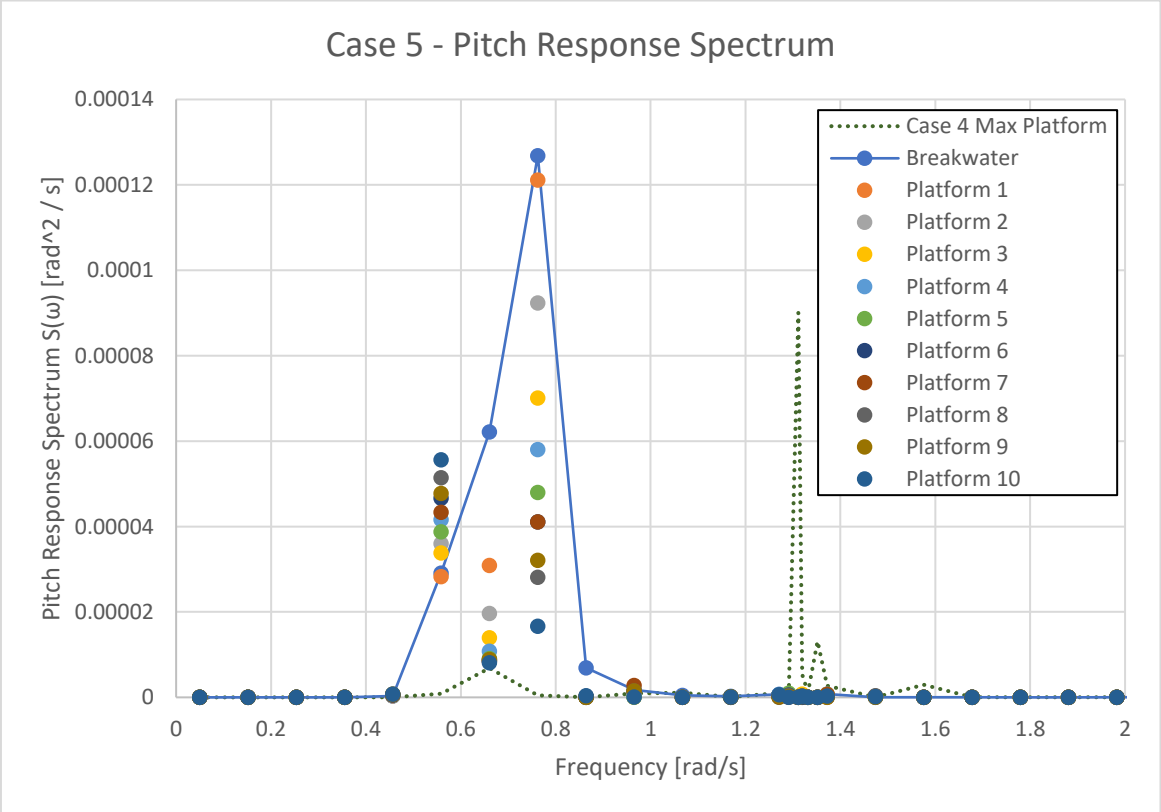

Figure 5.26: Case 5 Pitch Response Spectrum results in scatter plot. Case 4 Max Platform Response (dotted line), Breakwater (line)

5.7. Case 6: Changing gap between the platforms

Case 5 shows that changing the gap between the platforms removes the platform coupled natural frequencies at 0.18 rad/s and 1.3 rad/s. However, it does not remove the breakwater coupled natural frequency at 1.37 rad/s. This lends credence to the hypothesis that the former two frequencies were indeed due to hydrodynamic coupling between the platforms. In order to investigate further and better understand what might be happening, Case 6 changes the gap between platforms, marked as x in Figure 5.27, for a range of values from 5 m to 100 m. The dimensions of the breakwater and platforms and the gap between the breakwater and the first platform remain the same as in Case 5.

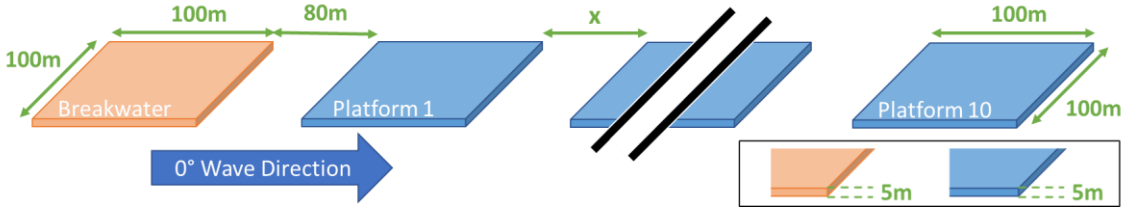

Figure 5.27: Schematic of model used in Case 6

Figure 5.28 and Figure 5.29 show the heave and pitch RAO results respectively for analysis from 0.05 – 3 rad/s with a step size of 0.1 rad/s with a higher resolution between 1.27 – 1.37 rad/s with a step size of 0.02 rad/s and an additional data point at 1.3 rad/s. Figure 5.30 and Figure 5.31 show the heave and pitch response spectrum respectively for the same frequencies. The results for 20 m (grey dashed line) and 80 m (green dashed line) are the Case 4 and Case 5 results respectively in all four figures. The heave response spectrum shown in Figure 5.30 also shows the wave spectrum in an orange dotted line.

The results show that the 10 m gap model shares the natural frequency at 1.37 rad/s with the 20 m (Case 4) and 80 m (Case 5) models. None of the other gap size models share the 1.3 rad/s natural frequency with the 20 m (Case 4) model. The 40 m, 60 m and 100 m gap models have reasonable RAOs in both heave and pitch, with the 100 m gap model having the best overall RAOs. The response spectrums, especially in pitch, show the 100 m gap model to be the best performing model overall.

The cause behind these observations cannot yet be accurately determined using the data available. Since, all the frequencies of interest are lower than 1.412 rad/s , irregular frequencies can be eliminated as a cause. Gap resonance could be another reason. The Heave-Pitch coupling was investigated for all frequencies between 0.05 – 2 rad/s that correspond to gap resonance wavelengths following $(n \times \lambda)/2 = 100$ m. However, no concrete trend of local maxima was found using the available data possibly due to inexact frequency analysis. Therefore, gap resonance cannot yet be rejected. Future analyses using pressure distribution and/or wave elevation might be able to provide the necessary explanations to the observations of this case. Using the results shown here, a gap of 100 m between the platforms is chosen as the recommendation since it has the lowest response in both heave and pitch overall.

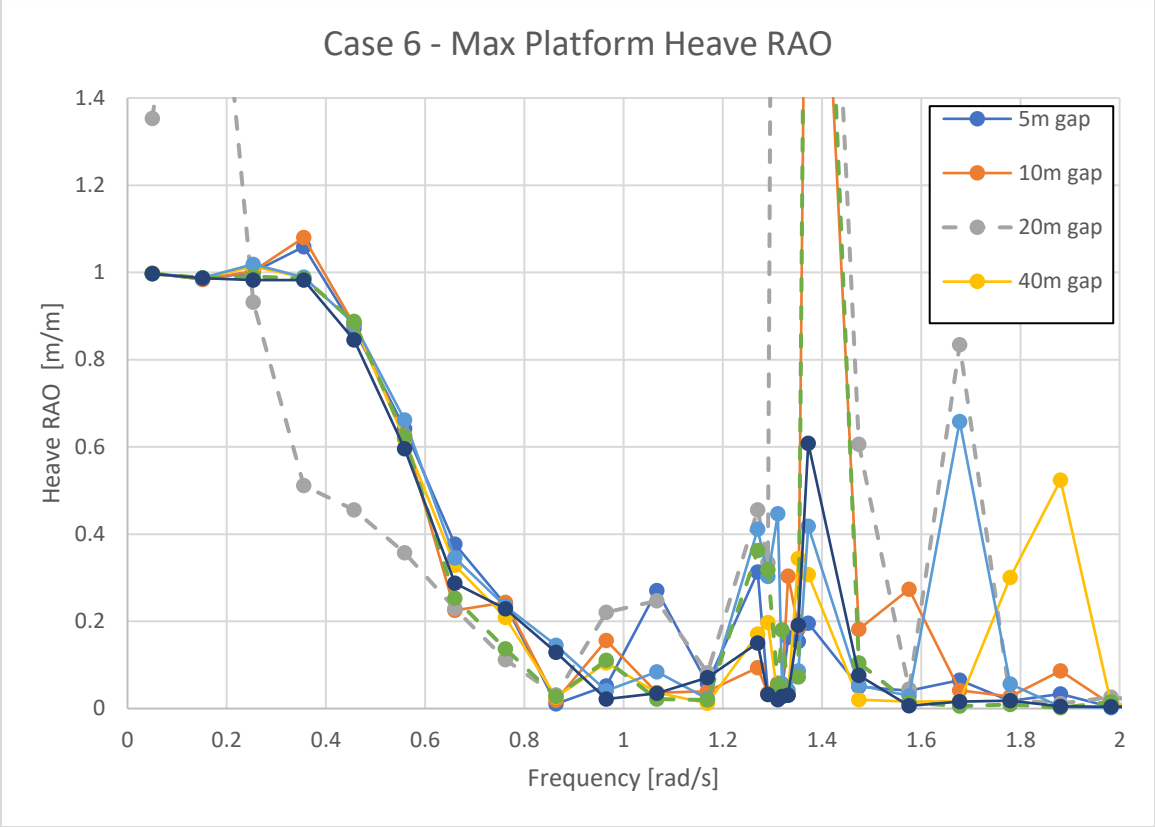

Figure 5.28: Case 6 Max Platform Heave RAO in scatter plot. Case 4/20m gap (gray dashed line), Case 5/80m gap (green dashed line)

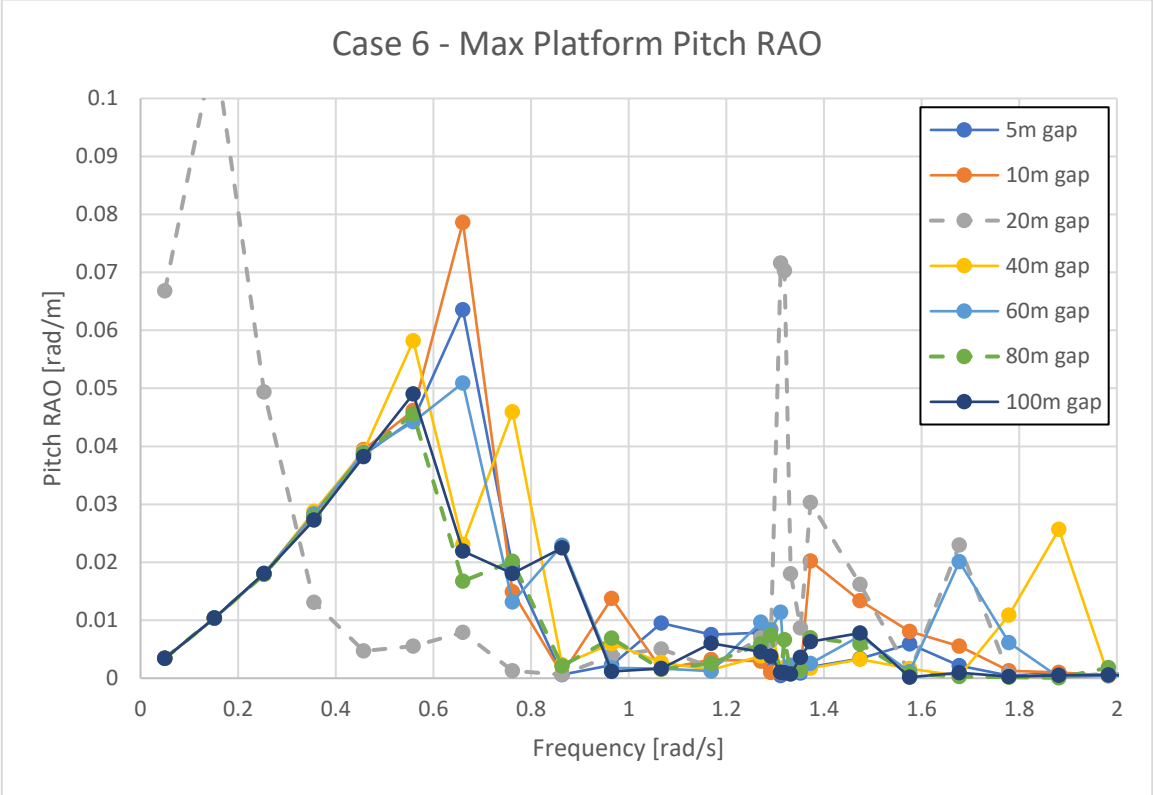

Figure 5.29: Case 6 Max Platform Heave RAO in Scatter plot. Case 4/20m gap (gray dashed line), Case 5/80m gap (green dashed line)

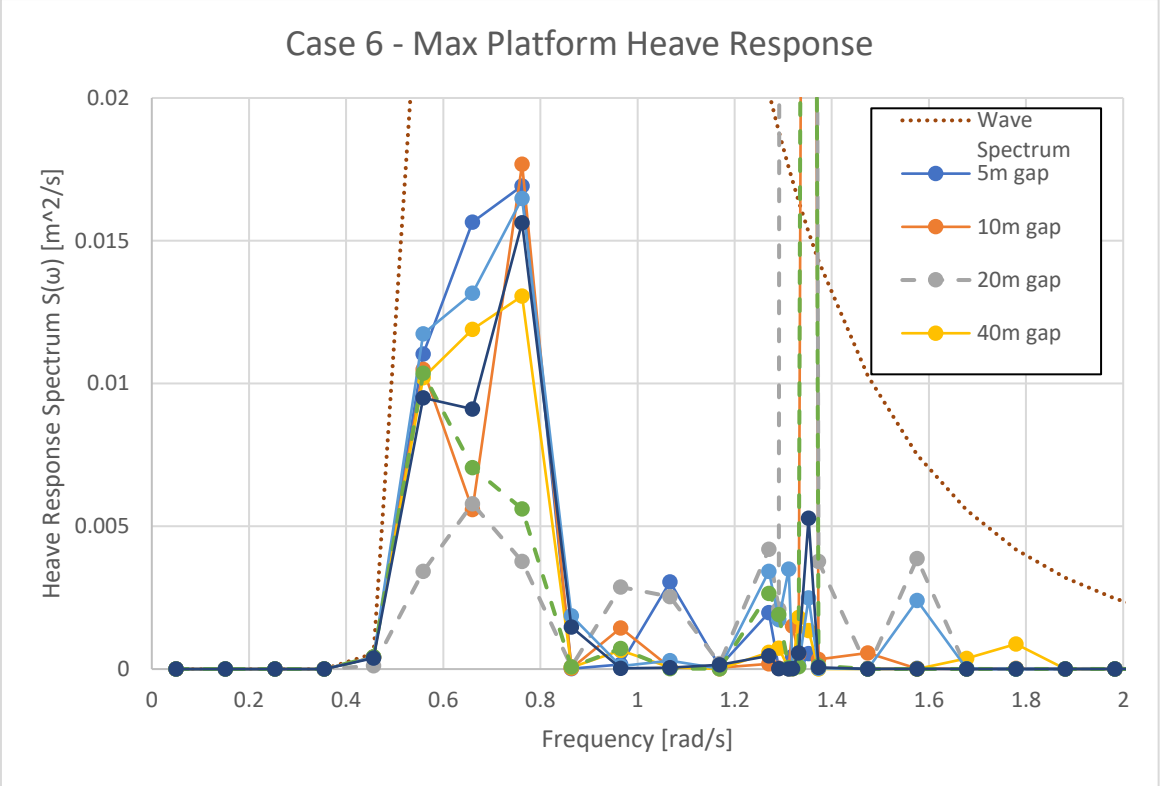

Figure 5.30: Case 6 Max Platform Heave Response Spectrum in scatter plot. Case 4/20m gap (gray dashed line), Case 5/80m gap (green dashed line)

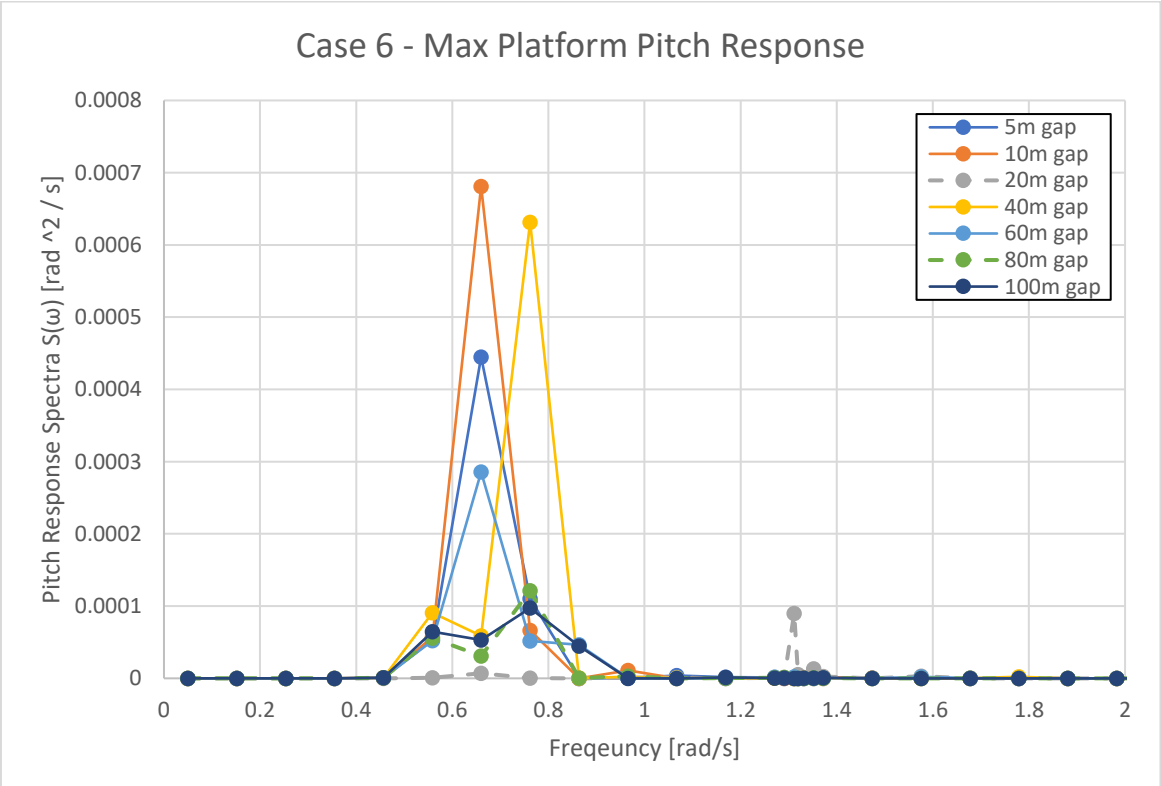

Figure 5.31: Case 6 Max Platform Pitch Response Spectrum in scatter plot. Case 4/20m gap (gray dashed line), Case 5/80m gap (green dashed line)

6. Conclusions and Recommendations

This thesis investigated the impact of the leading floating platform, functionally a breakwater, on the RAOs and response of the floating platforms behind it in frequency domain and in head waves only. The method was verified and validated for single body and multi-body hydrodynamically coupled systems.

The platforms were chosen to be square. An arbitrary site with a depth of 22 m was chosen. The platforms and breakwater dimensions were analysed for varying side length and draft. Base case dimensions for the platforms and breakwater were chosen based on the natural frequencies and wave transmission coefficients respectively. These choices were made based on the wave spectrum at the chosen site.

Variables in breakwater design were investigated. They were the gap between the breakwater and the first platform, the width, length of the side perpendicular to wave direction, of the breakwater and the gap between the platforms. Based on the results of analysing the variables in breakwater design, recommendations were made that would perform best at the chosen site. This recommended model was analysed for RAOs and response in heave and pitch primarily. Concerningly large response at some frequencies led to investigations into changing the gap between platforms such that large responses are avoided.

6.1. Conclusions

A breakwater and multiple platforms downstream of dimension $L = 100$ m, $B = 100$ m, $T = 5$ m, with a gap of 80 m between the breakwater and platforms and 100 m between the platforms themselves was shown to effectively reduce the motions of the downstream platforms. Some further conclusions are listed below.

i) For box-type breakwaters, the length of the structure, i.e. the side parallel to wave direction, followed by draft are the most influential dimensions in terms of wave transmission coefficient.

ii) The imperfect efficiency of a breakwater means that the first few platforms behind it act as breakwaters too. Albeit for much lower wave energies. Changing gap size had the largest impact on reducing the RAOs of the first platform behind the breakwater.

iii) Increasing the gap between the breakwater and the first platform behind it results in decrease in RAO of the platforms due to increasing hydrodynamic coupling. The impact on pitch RAOs is greater than the impact on the heave RAOs. 80 m is the recommended gap for the model analysed in this thesis.

iv) Increasing the width of the breakwater, i.e. the side perpendicular to wave direction, results in minimal reduction in RAOs of the platforms behind it at large gap sizes. At small gap sizes, there is an adverse relationship such that the RAOs of the platforms increase as the breakwater's width increases. The results in this thesis are inadequate to determine the cause of this adverse relationship.

v) Hydrodynamic coupling between the platforms can lead to shared natural frequencies within the design frequency range, leading to a large motion response. This can be prevented by changing the gap size and thereby the hydrodynamic coupling and moving the natural frequency outside of the design range. 100 m is recommended for the model analysed in this thesis.

The first few platforms exhibit higher heave than the other platforms, but similar pitch to the other platforms. Therefore, their use cases in a floating city must be chosen accordingly. The potential negative impacts of hydrodynamic coupling between the platforms means that the platforms must be further apart from each other, resulting in floating cities with a much larger footprint than previously expected.

6.2. Recommendations

This thesis covered a simplified analysis of the impact of box-type breakwaters on the platforms behind it. There are many relevant things that could be investigated in further studies.

i) Wave Directions & 2D Layout: This thesis only considers head waves and a single file arrangement of the structures. In reality, waves come from multiple directions and cities will most likely have more than a single line of platforms. Therefore, a 2D layout of structures and their response in different wave directions is worth investigating.

ii) Drift Forces & Moorings: In actual projects, moorings are a necessity to maintain position. Second order drift forces cannot be ignored. The current implementation can be considered reasonably close to the RAOs a slack moored system might show. However, time domain analysis with mooring are worth investigating.

iii) Hydroelasticity: Structures of large dimensions are invariably hydroelastic to some degree. Although this might be neglected for structures of the order of 100m, larger structures will require hydroelastic rather than rigid body analysis. The method introduced by (Sun, et al., 2018) will work well if built upon the current implementation.

iv) Hinges: Hinges have been shown to reduce the internal bending moments in the structure at the expense of larger RAOs (Yoon, et al., 2014) (Sun, et al., 2018). Coupled with hydroelastic analysis, the implementation of hinges allows investigations into balancing internal stresses and motions.

v) Other breakwater designs: There are a veritable cornucopia of floating breakwater designs that various researchers have investigated. The inaccuracy of NEMOH when dealing with thin elements (Penalba, et al., 2017) rules some of them out for analysis using the current implementation. However, ideas such a double box breakwaters and pontoon-type breakwaters are natural ideas for further investigation.

Bibliography

ABS, 1999. *Preliminary MOB classification guide,* s.l.: s.n.

Al-Solihat, M. K. & Nahon, M., 2015. *Mooring and hydrostatic restoring of offshore floating wind turbine platforms.* Montreal, Canada, s.n.

Ang, W.-T., 2007. *A Beginner's Course in Boundary Element Methods.* Boca Raton: Universal Publishers.

Banerjee, P. K., 1994. *The Boundary Element Methods in Engineering.* 2 ed. London: McGraw-Hill.

Bravo, J., 2018. Sustainable cities, human mobility and international migration. *Report of the Secretary-General for the 51st session of the Commission on Population and Development,* 2.Volume E/CN.9/2018/2.

Cosgrave, E., 2017. The future of floating cities – and the realities. *BBC Future,* 11.

Dai, J., Wang, C. M., Utsunomiya, T. & Duan, W., 2018. Review of recent research and developments on floating breakwaters. *Ocean Engineering; Volume: 158;,* pp. 132-151.

Department in Shipbuilding Research Centre of Japan (SRC), 2003. *What's Mega-Float?.* [Online]
Available at: http://www.srcj.or.jp/html/megafloat_en/menu/top.html
[Accessed 19 10 2020].

Du, S. X., Hudson, D. A., Geraint, P. W. & Temarel, P., 2012. An investigation into the hydrodynamic analysis of vessels with a zero or forward speed. *Journal of Engineering for the Maritime Environment,* 226(2), pp. 83-102.

Elchahal, G., Younes, R. & Lafon, P., 2009. Parametrical and Motion Analysis of a Moored Rectangular Floating Breakwater. *Journal of Offshore Mechanics and Arctic Engineering,* 131(031303).

Feng, X. & Bai, W., 2017. Hydrodynamic analysis of marine multibody systems by a nonlinear coupled model. *Journal of Fluids and Structures,* Volume 70, pp. 72-101.

Gold, M., 2018. Making space: Surviving sprawl. *The Economist - Intelligence Unit,* 7.

Gracey, W., 1941. *The additional-mass effect of plates as determined by experiments.,* s.l.: s.n.

Hong, D. C., Hong, S. Y. & Hong, S. W., 2006. Reduction of hydroelastic responses of a very-long floating structure by a floating oscillating-water-column breakwater system. *Ocean Engineering,* 4, Volume 33, pp. 610-634.

Hong, S., Choi, Y. & Hong, S., 2002. *Analysis of Hydro-elastic Response of Pontoon-type VLFS Coupled With Floating Breakwaters Using a Higher-Order Boundary Element Method.* Kitakyushu, Japan, International Society of Offshore and Polar Engineers.

Ikoma, T. et al., 2002. *Effects of submerged vertical plates and air chamber units in hydroelastic response reductions.* s.l., s.n.

Ikoma, T. et al., 2009. *Hydroelastic motion of aircushion type large floating structures with several aircushions using a three-dimensional theory.* s.l., s.n., pp. 1331-1338.

Inglis, R. & Price, W., 1981. Irregular frequencies in three dimensional source distribution techniques. *International Shipbuilding Progress,* Volume 28, pp. 57-62.

John, F., 1949. On the motion of floating bodies. I. *Communications on Pure and Applied Mathematics,* Volume 2, pp. 13-57.

John, F., 1950. On the motion of floating bodies II. Simple harmonic motions. *Communications on pure and applied mathematics,* Volume 3, pp. 45-101.

Kagemoto, H. & Yue, D. K. P., 1986. Interactions among multiple three-dimensional bodies in water waves: an exact algebraic method. *Journal of fluid mechanics,* Volume 166, pp. 189-209.

Kashiwagi, M., 1998. A B-spline Galerkin scheme for calculating the hydroelastic response of a very large floating structure in waves. *Journal of marine science and technology,* Volume 3, pp. 37-49.

Kashiwagi, M., 2004. Transient responses of a VLFS during landing and take-off of an airplane. *Journal of Marine Science and Technology,* 5, Volume 9, pp. 14-23.

Kashiwagi, M., Endo, K. & Yamaguchi, H., 2005. Wave drift forces and moments on two ships arranged side by side in waves. *Ocean Engineering,* 4, Volume 32, pp. 529-555.

Katsikadelis, J. T., 2002. *Boundary Elements Theory and Applications.* Amsterdam: Elsevier.

Lawther, A. & Griffin, M. J., 1988. Motion sickness and motion characteristics of vessels at sea. *Ergonomics,* 31(10), pp. 1373-1394.

LHEEA Centrale Nantes, 2017. *NEMOH-Theory.* [Online]
Available at: https://lheea.ec-nantes.fr/valorisation/logiciels-et-brevets/nemoh-theory
[Accessed 12 October 2020].

LHEEA Cetrale Nantes, 2017. *NEMOH-Presentation.* [Online]
Available at: https://lheea.ec-nantes.fr/research-impact/software-and-patents/nemoh-presentation
[Accessed 12 October 2020].

Macagno, E. O., 1953. *Fluid mechanics: experimental study of the effects of the passage of a wave beneath an obstacle..* s.l., Proceedings of the Academic des Sciences.

Maeda, H. et al., 2000. *Hydro-elastic response reduction system of a very large floating structure with wave energy absorption devices(Conference Paper).* s.l., s.n., pp. 527-531.

Mamidipudi, P. & Webster, 1994. *The motion performance of a mat-like floating airport.* s.l., s.n., pp. 363-375.

Maruo, H., 1960. The Drift on a Body Floating in Waves. *J. Ship Res.,* Volume 4, pp. 1-10.

Ohmatsu, S., 1998. *Numerical calculation of hydroelastic behavior of VLFS in time domain.* s.l., s.n., pp. 89-97.

Ohmatsu, S., 1999. Numerical calculation method of hydroelastic response of a pontoon-type VLFS close to a breakwater. *Journal of the Society of Naval Architects of Japan,* Volume 1999, pp. 193-199.

Ohta, H., 1999. *Effect of attachment of a horizontal/vertical plate on the wave response of a VLFS.* s.l., s.n., pp. 265-274.

Penalba, M., Kelly, T. & Ringwood, J., 2017. *Using NEMOH for Modelling Wave Energy Converters: A Comparative Study with WAMIT.* s.l., s.n.

Pinkster, J. A., 1979. Mean and low frequency wave drifting forces on floating structures. *Ocean Engineering,* 1, Volume 6, pp. 593-615.

Riola, J. & Garcia de Arboleya, M., 2006. Habitability and personal space in seakeeping behaviour. *Journal of Maritime Research,* 3(1), pp. 41-54.

Shigemitsu, H. et al., 2001. Feasibility study of reducing wave load on pontoon-type Mega-Float structure. *ASME Paper No. OMAE2001/OSU-5011.*

Summey, D., Smith, N., Watkinson, K. & Humphreys, D., 1978. *Hydrodynamic Stability and Control Analysis of GTOPS Vehicle,* Panama City FL.: NAVAL COASTAL SYSTEMS CENTER.

Sun, Y., Lu, D., Xu, J. & Zhang, X., 2018. A study of hydroelastic behavior of hinged VLFS. *International Journal of Naval Architecture and Ocean Engineering,* 3, Volume 10, pp. 170-179.

Suzuki, H. et al., 2006. *ISSC committee VI. 2: Very large floating structures.* s.l., s.n., pp. 394-442.

Takagi, K., Shimada, K. & Ikebuchi, T., 2000. An anti-motion device for a very large floating structure. *Marine Structures,* 7, Volume 13, pp. 421-436.

Tay, Z. Y., Wang, C. M. & Utsunomiya, T., 2009. Hydroelastic responses and interactions of floating fuel storage modules placed side-by-side with floating breakwaters. *Marine Structures,* 7, Volume 22, pp. 633-658.

The New Climate Economy, 2014. *Chapter 2: Cities,* s.l.: s.n.

United Nations, 2018. *68% of the world population projected to live in urban areas by 2050, says UN.* [Online]
Available at: https://www.un.org/development/desa/en/news/population/2018-revision-of-world-urbanization-

prospects.html
[Accessed 12 11 2020].

United Nations, 2019. Sustainable Floating Cities Can Offer Solutions to Climate Change Threats Facing Urban Areas, Deputy Secretary-General Tells First High-Level Meeting. *Press Release,* 4.Volume DSG/SM/1269-ENV/DEV/1936-HAB/248.

USNA, n.d. *Chapter 5 The Output: Ship Motions in Waves.* [Online]
Available at: https://www.usna.edu/NAOE/_files/documents/Courses/EN455/EN455_Chapter5.pdf
[Accessed 16 10 2020].

Utsunomiya, T., Watanabe, E., Nakamura, N. & others, 2001. *Analysis of drift force on VLFS by the near-field approach.* s.l., s.n.

Utsunomiya, T., Watanabe, E. & Taylor, R. E., 1998. *Wave response analysis of a box-like VLFS close to a breakwater.* s.l., s.n.

van Kessel, J. L. F. & Pinkster, J. A., 2007. *The Effect of Aircushion Division on the Motions of Large Floating Structures.* s.l., ASME.

Wang, C. M. & Tay, Z. Y., 2011. Very Large Floating Structures: Applications, Research and Development. *Procedia Engineering,* Volume 14, pp. 62-72.

Wang, C. M., Tay, Z. Y., Takagi, K. & T. Utsunomiya, 2010. Literature Review of Methods for Mitigating Hydroelastic Response of VLFS Under Wave Action. *Applied Mechanics Reviews,* Volume 63, p. 030802.

Wang, C. M., Watanabe, E. & Utsunomiya, T., 2006. *Very large floating structures.* s.l.:CRC Press.

Watanabe, E. et al., 2003. Wave response analysis of VLFS with an attached submerged plate. *International Journal of Offshore and Polar Engineering,* Volume 13.

Watanabe, E., Utsunomiya, T. & S, T., 1998. A transient response analysis of a very large floating structure by finite element method.. *Structural Engineering/Earthquake Engineering,* 15(2), pp. 155-163.

Watanabe, E., Utsunomiya, T., Wang, C. M. & Hang, L. T. T., 2000. Benchmark hydroelastic responses of circular VLFS under wave action. *Engineering Structures,* Volume 28, pp. 423-430.

Wehausen, J. V. & Laitone, E. V., 1960. Surface waves. In: *Fluid Dynamics/Strömungsmechanik.* s.l.:Springer, pp. 446-778.

Williams, A., Lee, H. & Huang, Z., 2000. Floating pontoon breakwaters. *Ocean Engineering,* 3, Volume 27, pp. 221-240.

Yago, K. & Endo, H., 1996. On the Hydoroelastic Response of Box-Shaped Floating Structure with Shallow Draft. *Journal of the Society of Naval Architects of Japan,* Volume 1996, pp. 341-352.

Yoon, J.-S., Cho, S.-P., Jiwinangun, R. G. & Lee, P.-S., 2014. Hydroelastic analysis of floating plates with multiple hinge connections in regular waves. *Marine Structures,* Volume 36, pp. 65-87.

Appendix A **Boundary Element Method**

Boundary Element Method (BEM) (Banerjee, 1994; Ang, 2007; Katsikadelis, 2002) is a numerical technique which uses the systems of partial differential equations formulated into equivalent boundary integral form. The method of Green's functions is used to transform the flow problem (domain integral equation) into a problem of source distribution on the body surface (boundary integral equation). BEM solves for the radiated and scatter velocity potentials arising from the interaction of the body located in a harmonic linear wave field and the field itself. The body is fixed in position to solve the scattering potential and the radiating potential is found by moving the body in the absence of incident waves. This can be resolved into components in phase with the velocity and acceleration of the body in order to determine the added-mass and radiation damping terms.

One can begin with the mathematical preliminaries for BEM, with variables as described in Appendix Figure A.1.

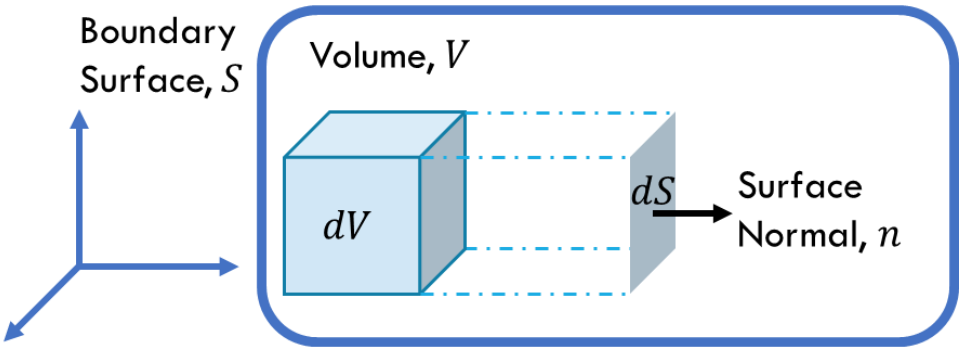

Appendix Figure A.1: Mathematical Preliminaries for BEM

Based on the Divergence Theorem shown in equation 0.1, Green's Second Theorem can be used in order to transform a domain integral equation into a boundary integral equation as shown in equation 0.2. Note that f, g in the latter equation are scalar functions while f in the former is a vector function.

$$\int_V (\nabla \cdot \mathrm{f}) dV = \int_S (\mathrm{f} \cdot n) dS \tag{0.1}$$

$$\int_V (f\nabla^2 \mathrm{g} - \mathrm{g}\nabla^2 f) dV = \int_S (f\nabla \mathrm{g} \cdot n - \mathrm{g}\nabla f \cdot n) dS \tag{0.2}$$

In other words, this reduces the problem from being a volumetric integral to surface integral, thereby reducing complexity. Another mathematical preliminary is Betti's Reciprocal Theorem that states that for any two loading conditions A and B, the following equation 0.3 holds true.

$$Force_A \ Displacement_B = Force_B \ Displacement_A \tag{0.3}$$

One can now begin formulating the BEM, starting with the Laplace equation, shown in equation 0.4, where ∇ is the nabla operator and u are the potentials. If internal sources exist, then the equation becomes the Poisson equation, shown in equation 0.5, where b are the sources.

$$\nabla^2 u = 0 \tag{0.4}$$

$$\nabla^2 u = b \tag{0.5}$$

One can now begin constructing a potential flow. If one assumes a Source point p_f and Field point p_f, as shown in Appendix Figure A.2, a Dirac delta source would be as shown in equation 0.6.

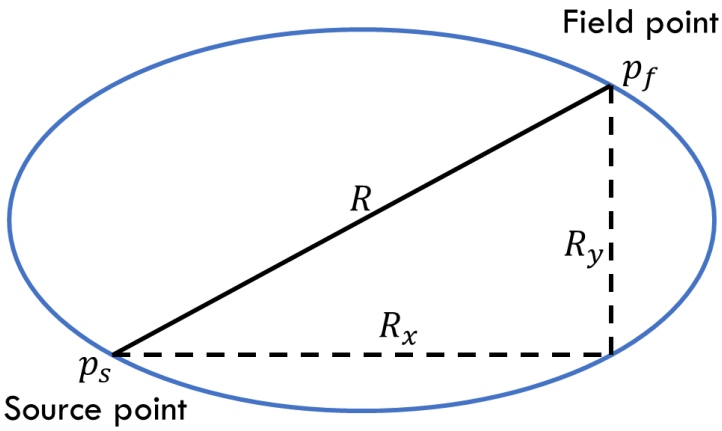

Appendix Figure A.2: Potential flow explanatory digram

$$\nabla^2 u^* = \delta(p_s), \qquad where\ \delta(p_s) = \begin{cases} \infty, at\ p_s \\ 0, others \end{cases} \tag{0.6}$$

The fundamental solution for the 2D and 3D case shall be as shown in equation 0.7 and equation 0.8 respectively.

$$2D:\ u^*(p_f) = \frac{1}{2\pi}\ln\left(\frac{1}{R}\right)\ and\ q^*(p_f) = \frac{-1}{2\pi R^2}\left(R_x n_x + R_y n_y\right) \tag{0.7}$$

$$3D:\ u^*(p_f) = \frac{1}{4\pi R}\ and\ q^*(p_f) = \frac{-1}{4\pi R^3}\left(R_x n_x + R_y n_y + R_z n_z\right) \tag{0.8}$$

If one then multiplies the fundamental solution u^* by the Laplace equation 0.4,

$$u^*(\nabla^2 u) = 0 \tag{0.9}$$

then multiply the potential u by the fundamental equation 0.6,

$$u(\nabla^2 u^*) = u\delta(p_s) \tag{0.10}$$

then subtract equation 0.9 from equation 0.10,

$$u(\nabla^2 u^*) - u^*(\nabla^2 u) = u\delta(p_s) \tag{0.11}$$

then integrating the equation 0.11 on a volume V,

$$\int_V [u(\nabla^2 u^*) - u^*(\nabla^2 u)]dV = \int_V u\delta(p_s)\, dV \tag{0.12}$$

then using Green's second identity (equation 0.2),

$$\int_S [u^*\nabla u \cdot n - u\nabla u^* \cdot n]dS = \int_V u\delta(p_s)dV = c(p_s)u(p_s) \tag{0.13}$$

and therefore $c(p_s)$ is a coefficient at p_s such that,

$$if\ p_s\ is\ located \begin{cases} in\ the\ domain, c(p_s)\ should\ be\ 1 \\ on\ the\ smooth\ boundary, c(p_s)\ should\ be\ 0.5 \\ out\ of\ the\ domain, c(p_s)\ should\ be\ 0 \end{cases} \tag{0.14}$$

Note that since $\nabla u \cdot n = q$, the boundary integral equation can be written as,

$$\int_S (u^* q_n - q_n^* u)dS = c(p_s)u(p_s) \tag{0.15}$$

The boundary can now be discretized into elements and interpolated using shape functions N, $u = \sum N_i \hat{u_i}$ and $q = \sum N_i \hat{q_i}$ where $\hat{u_i}$ and $\hat{q_i}$ are the i^{th} nodal values of potential and velocity at the boundary respectively.

$$c(p_s)u(p_s) + \sum_{element} \int_{S_e} q_n^* N\, dS_e\, \hat{u} = \sum_{element} \int_{S_e} u^* N\, dS_e\, \widehat{q_n} \tag{0.16}$$

Appendix B **BEM/NEMOH Assumptions**

This method assumes that each module was rigid. Assumptions made with this method are as follows (Sun, et al., 2018):

(1) The fluid is incompressible, irrotational and inviscid.

(2) The incident wave amplitude is assumed to be small relative to the structures such that linear Airy wave theory can be applied.

One can begin this explanation with a schematic that defines the fluid and structure boundaries as shown in Appendix Figure B.1. The figure shows a multi-module setup with m modules in a fluid domain Ω, with free surface S_F, bottom surface S_B and boundary surface S_∞ at infinity of the fluid.

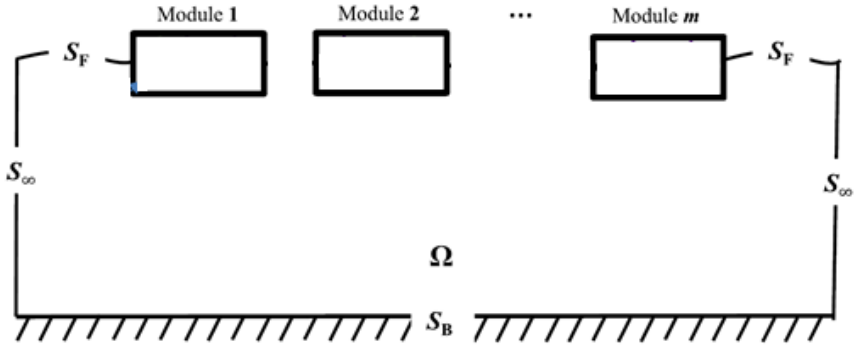

Appendix Figure B.1: Definition of structure and fluid boundaries

One can then begin describing the fluid with the velocity potential that can be decomposed into three parts as shown in equation below based on the assumption of an ideal fluid and linearity.

$$\phi = \phi_I + \phi_D + \phi_R \tag{0.17}$$

The three parts denoted by ϕ_I, ϕ_D and ϕ_R refer to incident wave potential, diffraction wave potential and radiation wave potential respectively. They satisfy the following boundary conditions:

$$\begin{cases} \nabla^2\phi = 0, & in\ \Omega \\ -\omega^2\phi + g\dfrac{\delta\phi}{\delta z} = 0, & on\ S_F \\ \dfrac{\delta\phi}{\delta z} = 0, & on\ S_B \\ \dfrac{\delta(\phi_1 + \phi_D)}{\delta z} = 0, & on \sum_{q=1}^{m} S_q \\ \dfrac{\delta\phi_{Rk}}{\delta n_k} = \overrightarrow{V_{S_k}} \cdot \overrightarrow{n_k}, & on\ S_k (k = 1,2,\dots,m) \\ \dfrac{\delta\phi_{Rk}}{\delta n_j} = 0, & on \sum_{j=1, j\neq k}^{m} S_j \\ \lim\limits_{r\to\infty} \sqrt{r}\left(\dfrac{\delta\phi_{Rk}}{\delta r} - \dfrac{i\omega^2}{g}\phi_{Rk}\right) = 0, & on\ S_\infty \end{cases} \tag{0.18}$$

where S_k and S_j represent the wetted body surface of the kth and jth module respectively such that $(k, j = 1,2, \dots, m; j \neq k)$; $\overrightarrow{n_k}$ represents the outwards directed unit vector normal to the wetted surface of the kth module, $\overrightarrow{V_{S_k}}$ is the velocity of a given point on the wetted surface of the kth module; ϕ is the velocity potential that can be replaced by ϕ_I, ϕ_D or ϕ_R and r is the distance between the source point and the far-field point. The excitation forces and added mass and radiation damping can now be calculated in the frequency domain.